Novel Co 2+ and Cd 2+ Complexes Derived From a New N -Donor Pyridyl-Functionalized Thiophosphoric Triamide Ligand: Structural Investigation, DNA/COVID-19/Monkeypox Molecular Docking, and Biological Assays

Zeinab Albobaledi, Atekeh Tarahhomi, Ali Khaleghian, Arie van der Lee, Grégory Excoffier

Novel Co^{2+} and Cd^{2+} complexes derived from a new *N*-donor pyridyl-functionalized thiophosphoric triamide ligand: structural investigation, DNA/COVID-19/Monkeypox molecular docking, and biological assays

Zeinab Albobaledi[1], Atekeh Tarahhomi[1,*], Ali Khaleghian[2], Arie van der Lee[3], Grégory Excoffier[4]

[1]Department of Chemistry, Semnan University, Semnan 35351-19111, Iran

[2]Faculty of Medicine, Biochemistry Department, Semnan University of Medical Sciences, Semnan, Iran

[3]IEM, Université de Montpellier, CNRS, ENSCM, Montpellier, France,

[4]Aix Marseille Univ, CNRS, Centrale Marseille, FSCM, Spectropole, Marseille, France

Corresponding author: Atekeh Tarahhomi, E-mail address: tarahhomi.at@semnan.ac.ir

Tel.: +98 23 31533199; fax: +98 23 33654110

A thiophosphoric triamide (SPT) ligand P(S)[NH-^{2}Py]$_3$ was synthesized and utilized as a ligand to make novel bi- and mono-nuclear Co^{2+} and Cd^{2+} complexes. The complexes are the first examples of discrete chelate thiophosphoric triamide (SPT) with an [N]$_3$P(S)-based backbone in which the SPT acts as a flexible tridentate *N*,*N*,*N*-donor or *N*,*N*,*O*-donor ligand. The metal cation features a hexa-coordinate environment M(N)$_3$(Cl)$_3$ / M(N)$_4$(O)$_2$ adopting a distorted octahedral geometry. Hirshfeld surface analysis affirms that the pyridinyl nitrogen is a more dominant H-bond acceptor than the thiophosphoryl sulfur atom. The inhibitory activity against MDA-MB-231 cancer cell line was *in vitro* indicated good inhibitory effect for all compounds. The mononuclear Co^{2+} complex showed stronger inhibitory activity against cancer cells than other studied compounds with an IC50 of 62 ± 1.4 nmolar. Antioxidant and anti-hemolytic activity of the compounds showed appreciable performance with the highest activities for the Cd^{2+} complex. A computational DNA binding study by molecular docking indicated a good affinity of the compounds with the DNA receptor by a mixed mode of interactions. Docking was also performed on SARS-CoV-2 and Monkeypox (Mpox) resulting in binding energies (–5.5 kcal/mol to –8.9 kcal/mol) which are competitive with current effective drugs.

KEYWORDS

Thiophosphoramide, X-ray crystallography, Anticancer, SARS-CoV-2, Monkeypox, Molecular docking.

1 INTRODUCTION

Thiophosphoramides, a class of amino-functionalized P(V) derivatives containing a thiophosphorous imido bond (S═P–N) are interesting compounds which have recently attracted a great deal of interest owing to their widespread use in medicine as prodrugs, anticancer, antiviral, and antioxidants[1], and in agricultural industry as insecticides and antifungal[2]. The particular coordination chemistry of thiophosphoramide compounds and their use as ligand lead to promising properties such as photoluminescence, thermochromism and magnetic behavior[3]. The P═S unit of such ligands does mostly not participate in the coordination to the metal ions, especially in the case of hard metals. The use of suitable substituents such as trishydrazone and aminopyridine embarked on the thiophosphoryl group can provide the structural supports to form multi-site coordination ligands and in result, multi-nuclear complexes and metal–organic frameworks (MOFs)[4].

Identifying new compounds with potential bioactivity and evaluating their use as drugs in the treatment of diseases are still one of most important challenges in different fields of medicine, chemistry and pharmacology. Evaluation of novel bioactive compounds by using clinical trials and traditional approaches is often difficult and time-consuming. Computer-aided drug discovery may, however, facilitate and accelerate this assessment process. Moreover, the understanding of the structural aspects of the bioactive compounds by using X-ray diffraction techniques may provide valuable information about various intermolecular interactions directing the molecular architectures in a crystal structure and influence their connections with active sites of the biological targets[5].

Despite many efforts to elaborate effective drugs against corona and monkeypox (Mpox) viruses confident and decisive drugs have yet not been found up to now[6]. Treatments against different types of cancer also need to be developed with dugs having high sensitivity toward cancer cells and low toxic side effects. Most molecules proposed as anticancer drugs interact directly with DNA or disturb the DNA functions where the binding strength between the anticancer molecule with DNA is related to its biological activity. Thus, the investigation of the binding of candidate molecules with DNA is a reliable strategy to screen drugs[7].

In order to assist to identify new bioactive compounds, inhere we present the molecular docking and pharmacophore studies on new pyridyl-functionalized thiophosphoric triamide (S)P[NH-^{2}Py]$_3$ ligand and three novel Co^{2+} and Cd^{2+} complexes derived from it, where our focus was on cancer, corona and Mpox diseases above-mentioned. The structures of these compounds were studied by single crystal X-ray diffraction analysis. A Hirshfeld surface analysis was also carried out for all compounds to further investigate intermolecular interactions and molecular assemblies.

2 EXPERIMENTAL

2.1 Materials and measurements

All solvents and chemicals used in this investigation paper were received from commercial sources. The melting points of compounds were obtained by an Electrothermal IA-9100 device. The Fourier-transform infrared spectra (FT-IR) of the compounds were performed by a KBr tablet with a SHIMADZU FT-IR device. Elementar Vario EL III elemental analyzer was also used for the elemental analyses (C, H, and N).

2.2. Syntheses and crystallization

2.2.1 Preparation of (S)P[NH-^{2}Py]$_3$ (1). To a solution of 2-aminopyridine (3.39 gr, 36.00 mmol) in dry toluene (15 mL) at 0 °C, a solution of thiophosphoryl chloride (1.02 gr, 6.00 mmol) in 5 mL of dry toluene was dropwise added and stirred for 30 min. The resulting mixture was refluxed for 4 h. The obtained solid was filtered and, it was purified several times with water after drying to remove the amine hydrochloride by-product. Colorless prismatic single crystals suitable for crystal structure determination were grown by slow evaporation solvents from a solution of **1** in ethanol (15 mL) at room temperature. **Yield**: 52% (1071 mg); **MP**: 210°C; **FT-IR Data (KBr, $\bar{\nu}$, cm^{-1}):** 3095 (N—H), 3078, 2961, 2845, 1596, 1571, 1483, 1442, 1406, 1292, 1267, 1157, 995, 954, 927 (P═S), 769 (P—N), 665, 474; **Anal. Calcd.** for $C_{15}H_{15}N_6PS$: C, 52.57; H, 4.38; N, 24.53; Found: C, 50.46; H, 3.87; N, 24.47.

2.2.2 Preparation of {(S)P[NH-^{2}Py]$_3$}(Cl)Co^{2+}Cl$_2$Co^{2+}(Cl){[NH-^{2}Py]$_3$P(S)} (2). In order to synthesize the Co^{2+} complex **2**, to a solution of the ligand (S)P[NH-^{2}Py]$_3$ (**1**) (2.00 gr, 6.00 mmol) in acetonitrile (15 mL), a solution of $CoCl_2.6H_2O$ (0.70 gr, 3.00 mmol) in methanol (10 mL) was dropwise added, and the reaction was stirred under reflux conditions for 2 days. The violet prism crystals were recrystallized from a solution of **2** in CH_3OH/DMSO (with volume ratio 3:1) by slow evaporation of the solvents at room

temperature. **Yield:** 68% (1877 mg); **MP:** 262°C; **FT-IR Data (KBr, $\bar{\nu}$, cm^{-1}):** 3240 (N—H), 3142, 2842, 1630, 1591, 1528, 1448, 1381, 1367, 1275, 1161, 1009, 974, 903 (P═S), 768 (P—N), 669, 463; **Anal. Calcd.** for $C_{30}H_{30}Cl_4Co_2N_{12}P_2S_2$: C, 55.90; H, 3.17; N, 17.78; Found: C, 53.08; H, 4.10; N, 15.51.

2.2.3 Preparation of [Co^{2+}{[O][NH-^{2}Py]$_2$P(S)}$_2$](DMSO) (3). The Co^{2+} complex **3** was obtained using a similar reaction as that for the synthesis of **2** involving (S)P[NH-^{2}Py]$_3$ (**1**) (0.10 gr, 0.30 mmol) solved in acetonitrile and $CoCl_2.6H_2O$ (0.03 gr, 0.15 mmol) solved in methanol. The clear solution was stirred at room temperature for 30 minutes followed by reflux conditions for 2 days. The pink prism crystals of **3** were grown from a solution of **3** in CH_2Cl_2/CH_3CN/DMSO (3:3:1) by slow evaporation of the solvents at room temperature. **Yield:** 46 (50 mg); **MP:** 270°C ; **FT-IR Data (KBr, $\bar{\nu}$, cm^{-1}):** 3236 (N—H), 3136, 2860, 1610, 1575, 1473, 1454, 1326, 1122, 1099, 1027, 921 (P═S), 775 (P—N), 702, 495; **Anal. Calcd.** for $C_{20}H_{20}CoN_8O_2P_2S_2.C_2H_6OS$: C, 35.40; H, 3.48; N, 15.09; Found: C, 34.08; H, 3.07; N, 16.51.

2.2.4 Preparation of {(S)P[NH-^{2}Py]$_3$}(Cl)Cd^{2+}Cl$_2$Cd^{2+}(Cl){[NH-^{2}Py]$_3$P(S)} (4). The Cd^{2+} compound **4** was prepared from a reaction between the SPT ligand **1** and the chloride salt of cadmium in such a way that the (S)P[NH-^{2}Py]$_3$ (**1**) (0.10 gr, 0.30 mmol) was dissolved in dichloromethane (20 ml) and the obtained cloudy solution was added to a solution of $CdCl_2.H_2O$ (0.06 gr, 0.30 mmol) in ethanol (5 mL). Ethanol (10 mL) was added to this mixture and the cloudy solution was stirred under reflux conditions for 4 hours. The mixture was filtered and the obtained clear solution was kept at room temperature for crystallization. Yellow prism crystals were obtained after about 1.5 months. **Yield:** 39% (60 mg); **MP:** 250°C; **FT-IR Data (KBr, $\bar{\nu}$, cm^{-1}):** 3254 (N—H), 3121, 2886, 1631, 1600, 1581, 1523, 1446, 1375, 1271, 1002, 964, 906 (P═S), 765 (P—N), 665; **Anal. Calcd.** for $C_{30}H_{30}Cd_2Cl_4N_{12}P_2S_2$: C, 68.48; H, 5.70; N, 31.95; Found: C, 64.08; H, 5.86; N, 32.05.

2.3 Crystal structure determination

Crystal evaluation of **1** – **4** and their X-ray diffraction data collection were conducted with the *CrysAlisPro* software package[8] on an Rigaku Oxford-Diffraction dual Supernova diffractometer equipped with a graphite-monochromated Cu-*Kα* (λ = 1.5405 Å) X-ray source. The same package was used for integration of the data using default parameters, correction for Lorentz and polarization effects, and for empirical absorption correction using spherical harmonics employing symmetry-equivalent and redundant data. The structures were solved

using the ab initio iterative charge flipping method with parameters described elsewhere[9], with use of the *SUPERFLIP* program[10]. The structures were then refined on $|F|^2$ using full-matrix least-squares procedures as implemented in *CRYSTALS*[11] on all independent reflections with $I > -3\sigma(I)$. In the absence of significant anomalous scattering, Friedel pairs were merged. The H atoms were all located in a difference map, but those attached to carbon atoms were repositioned geometrically. The H atoms were initially refined with soft restraints on the bond lengths and angles to regularise their geometry (C─H in the range 0.93 – 0.98 Å and N─H in the range 0.86 –0.89 Å) and U_{iso}(H) (in the range 1.2–1.5 times U_{eq} of the parent atom), after which the positions were refined with riding constraints[12]. Moreover, for **3**, the disorder of the sulfur atom and two methyl CH_3 groups at the solvent molecule O═S$(CH_3)_2$ (DMSO) was found and two discrete populations are defined with the occupancy 64/36%. The *PLATON*[13] and *Mercury*[14] programs were utilized for making the ORTEP and packing diagrams.

2.4 Hirshfeld surface (HS) analysis

The Crystal Explorer package[15] was employed to generate the graphical three-dimensional (3D) HS[16] maps and their associated two-dimensional (2D) fingerprint plots (FPs)[17] in order to evaluate intermolecular interactions in the studied structures. Molecular HSs were mapped over the d_{norm} property in which the red, white and blue coloring codes display contacts with distances shorter, equal and longer than the sum of van der Waals radii, respectively[18]. Surface maps with the shape-index property were also utilized to identify the C─H…π and π…π stacking highlighted by the presence of the red π-hole and the adjacent red and blue triangle patterns, respectively[19]. Moreover, the atoms propensity to form contacts in crystal was determined by calculating the enrichment ratio (E), where a high propensity to form contacts is called favored when E is larger than 1 and a low propensity is called (disfavored) when $E < 1$[20].

2.4 Biological studies

2.4.1 Cell culture

MDA-MB-231 cell lines (breast cancer) which are the type of cells that adhere to the bottom of the culture vessel were used to evaluate the cytotoxicity effect of the new complexes. The studied cells were cultured in a 96-multiwell plate in RPMI-1640 culture medium containing 100 μg/ml penicillin/streptomycin and 10% fetal bovine serum (FBS) to control the growth of

bacteria. EDTA trypsin solution was used to separate the cells from the flask. Cell counting was performed by using a hemocytometer slide. The percentage of living cells was calculated using trypan blue dye and it was always above 90%. The cells were incubated in an incubator at 37 degrees Celsius and had 5% carbon dioxide. Incubation in these conditions was continued until the cells reached a certain density (around eighty percent of the flask). Then, cytotoxic evaluation was performed against the studied cells (MD-MBA-231 cell line) and treatment was done using different concentrations of the synthesized compounds.[21]

2.4.2 Cytotoxic evaluation

To evaluate of the studied compounds **1** – **4** against the MD-MBA-231 cell line, different concentrations of those (12.5 nM - 100 nM) were added to each well. The plate containing the cells was placed in an incubator at 37°C for 48 hours. After 2 days, 10 µL of MTT (0.005 g in 1000 µL of phosphate buffered saline) was added to the wells and incubated at 37°C for 3-4 hours. Then the medium was removed from the plate, and 100 µL of Dimethyl Sulfoxide was added to each well. The plate was placed in an incubator for 5 minutes to dissolve the purple formazan crystals. The intensity of the formazan color was investigated by measuring the OD (Optical Density) at a wavelength of 570-590 nm using a spectrophotometer. Because MTT reagent is sensitive to light, this method is performed in the dark. Here, 5-FU (5-fluorouracil) was used as the standard drug. The absorption values of wells were presented as the percent of cell viability. The 50% inhibitory concentration (IC50) of the compounds was calculated via MTT assay[22].

2.4.3 DPPH radical scavenging assay

The 2,2-diphenyl-1-picrylhydrazyl (DPPH) method was used to check the free radical inhibition power of the synthesized compounds. Stock solutions were prepared by dissolving 0.001 g of ascorbic acid (as a standard drug) and each of the compounds in 1 ml of methanol, as well as dilute solutions of the complexes (3.90, 7.81, 15.62, 31.25, 62.5, 125 $\mu g/ml^{-1}$) in methanol. 300 µl of DPPH solution (0.004%) was mixed with 100 µl of sample and 1600 µl of methanol separately inside the test tube. The obtained mixture was well shaken and placed in the dark at room temperature for 20-30 minutes. The color of solutions changed from purple to yellow and their absorbance was read at a wavelength of 517 nm. This color change along with a low absorption confirms the good activity of the studied compounds to inhibit free radicals. In the case of ascorbic acid, which was used as a standard drug, the purple radical DPPH color disappears immediately due to its very high inhibitory activity. Thus, the

average absorbance was reported for each concentration. DPPH radical scavenging ability as radical scavenging activity (RSA%) was obtained using the following equation:

$$\text{Scavenging activity (\%)} = 100 \times (1 - (A_{sample}/A_{control}))$$

In the above equation, $A_{control}$ refers to the absorption of the control solution and A_{sample} refers to the absorption of the synthesized compounds. The EC_{50} values of the compounds were obtained from the graph of inhibitory activity (%) versus concentration. A low EC_{50} value indicates a high ability of compound to scavenge DPPH[23].

2.4.4 Anti-hemolytic assay

The anti-hemolytic effect of the studied compounds **1** – **4** was evaluated by in vitro method. Human red blood cells were washed for 6 minutes with physiological serum (0.9 g of sodium chloride in 100 ml of water) and centrifuged. The supernatant was removed. Then the red blood cells were diluted with physiological serum and a 5% suspension was obtained. Similar amounts of compounds (125 and 62.5 μg/mL) with physiological serum were added to 2 mL of red blood cell suspension. Then a specific concentration of hydrogen peroxide solution (3%) was prepared and added to distilled water. The obtained mixture was incubated at 37°C for 2 hours. The concentration of H_2O_2 was adjusted so that after 2 hours of incubation, 90% hemolysis of blood cells was obtained. Incubation was terminated after this time by centrifugation for 10 minutes at 1000 RPM. It should be noted that ascorbic acid was used as a control in this test. Also, the amount of hemolysis was determined by the amount of absorbance at the wavelength of 540 nm related to the release of hemoglobin. The experiments were repeated twice. Hemolysis inhibition was obtained from the following relationship[24].

$$\text{\% Inhibition of hemolysis} = \frac{\text{Absorbance of control} - \text{Absorbance of sample}}{\text{Absorbance of control)}} \times 100$$

2.5 Molecular docking procedure

Molecular docking simulation was employed to study the anti-cancer, anti-coronavirus and anti-monkeypox activities of the studied compounds. For this purpose, the crystal structures of B-DNA dodecamer (with PDB ID of 1BNA), DNA-Bound Human Topoisomerase II Alpha (1BNA and 4FM9), SARS-CoV-2 virus receptor (6M03 and 6LU7), and Monkeypox virus receptor (4QWO and 8CER) were obtained from the protein data bank (http://www.rcsb.org./pdb). Crystallographic data of the compounds **1** – **4** were also taken as a Crystallographic Information File (CIF), and converted to the PDB format by using

Discovery Studio 2021 client software[25]. Then, the water molecules in the ligands (the studied compounds **1** – **4**) and receptors were removed by the same software. The molecular docking was performed with AutoDock 4.2 and AutoGrid4.exe[26]. For the molecular docking simulation, polar hydrogen atoms, Gasteiger partial charges, and Kollman atomic type charges were added to the receptor. The simulations were performed on a grid box of 126 × 126 × 126 Å with a grid-point spacing of 0.564 Å for BNA, 126 × 126 × 126 Å / 0.736 Å for 4FM9, 98 × 120 × 122 Å / 0.447 Å for 6M03, 126 × 126 × 126 Å / 0.753 Å for 6LU7, 120 × 120 × 120 Å / 0.408 Å for 4QWO and, 92 × 126 × 126 Å / 0.847 Å for 8CER. Then GPF (Grid Parameter File), and DPF (AutoDock Docking Parameter File) files were created and Lamarckian genetic algorithm was used. The number of genetic algorithm executions was set to 100-200. After that, the interactions of the selected receptors and their binding modes with the compounds were analyzed using the AutoDock program, and Discovery Studio 2021 client.

3 RESULT AND DISCUSSION

3.1 Description of IR data

In the IR spectrum of **1**, the absorption band at 927 cm^{-1} is assigned to the P═S stretching band; such stretching frequencies were also reported for the similar thiophosphoric triamide compounds[27]. For the IR spectra of the metal complexes **2** – **4**, the P═S stretching frequencies (903 cm^{-1} for **2**, 921 cm^{-1} for **3** and 906 cm^{-1} for **4**) display a red shift relative to the free ligand **1** (927 cm^{-1}). However, the P═S group in both free ligand **1** and the metal complexes **2** – **4** is involved in the N─H···S═P hydrogen bond interaction. The reason for this red shift of the P═S stretching frequencies for the metal complexes **2** and **4** can be attributed to the coordination of the N─H groups as negative nitrogens to metal which replaces the stronger M─N interaction in the complexes with the N─H···N hydrogen bond interaction in the free ligand. The presence of these negative nitrogens connected to metal atoms in the coordinated (S)P[NH-^{2}Py][N^{-}-^{2}PyH]$_2$ ligands of **2** and **4** and their electron-withdrawing effect on the thiophosphoryl group lead to a decrease in the P═S stretching frequencies in the metal complexes. In the case of the Co^{2+} complex **3**, such electron-withdrawing effect on the P═S unit and its frequency reduction is caused by the negative oxygen in the (S)P[NH]$_2$[O^{-}]-based ligand coordinated to metal. Moreover, for the free ligand **1**, the stretching frequencies of three N─H units involved in the N─H···S═P and N─H···N hydrogen bond interactions appear at about 3200 cm^{-1}, whereas for the complexes **2** – **4**, the N─H stretching modes are

found at slightly higher frequencies (3240, 3236 and 3254 cm^{-1}, respectively, for **2** – **4**). This can be attributed to this fact that the N─H unit of **2** – **4** only takes part in the N─H···S═P hydrogen bond interaction and N─H···N hydrogen bonds are absent in these complexes. However, for **3**, the N─H···O hydrogen bond interaction is also observed between the N─H unit of the coordinated ligand with the oxygen atom of solvent.

3.2 Description of the structures

The details of the crystal data of the synthesized compounds along with the structure refinements are listed in Table 1. Selected bond angles and bond lengths are collected in Table S1. Table 2 presents the intermolecular interactions geometries for all compounds. The chemical structures and synthesis reactions of the studied structures **1** – **4** are shown in Scheme 1.

We have recently published studies on the pyridyl-functionalized phosphoric triamide complexes with a O═P[─N]$_2$[N/O] backbone and also their structural, electronic and antiviral properties[28]. For the current study we have synthesized new complexes of amino-functionalized P(V) derivatives containing a thiophosphoryl group with a S═P[─N]$_2$[N/O] backbone. We report the structures of the new tris(pyridin-2-yl)thiophosphoric triamide ligand (S)P[NH-^{2}Py]$_3$ (**1**) and three novel Co^{2+} and Cd^{2+} complexes derived from it: [M(Cl)(μ_2-Cl){(S)P[NH-^{2}Py][N-^{2}PyH]$_2$}]$_2$ (M = Co^{2+} (**2**) and Cd^{2+} (**4**)), and [Co^{2+} {[O][NH-^{2}Py]$_2$P(S)}$_2$](DMSO) (**3**) (Scheme 1). According to a Cambridge Structural Database survey (CSD, version 5.45, with November 2023 update)[29] these complexes are the first examples of a metal–ligand coordination compound for (S)P[NH-^{2}Py]$_3$ and also the first examples of discrete chelate complexes using from (S)P[NH-^{2,3,4}Py]$_3$ as a complexing agent. Compounds **2** and **4** are centrosymmetric binuclear neutral complexes, where for the first time a S═P[─N→]$_3$M coordination with trident thiophosphoric triamide (SPT) ligand is found, while **3** displays a centrosymmetric discrete mononuclear complex.

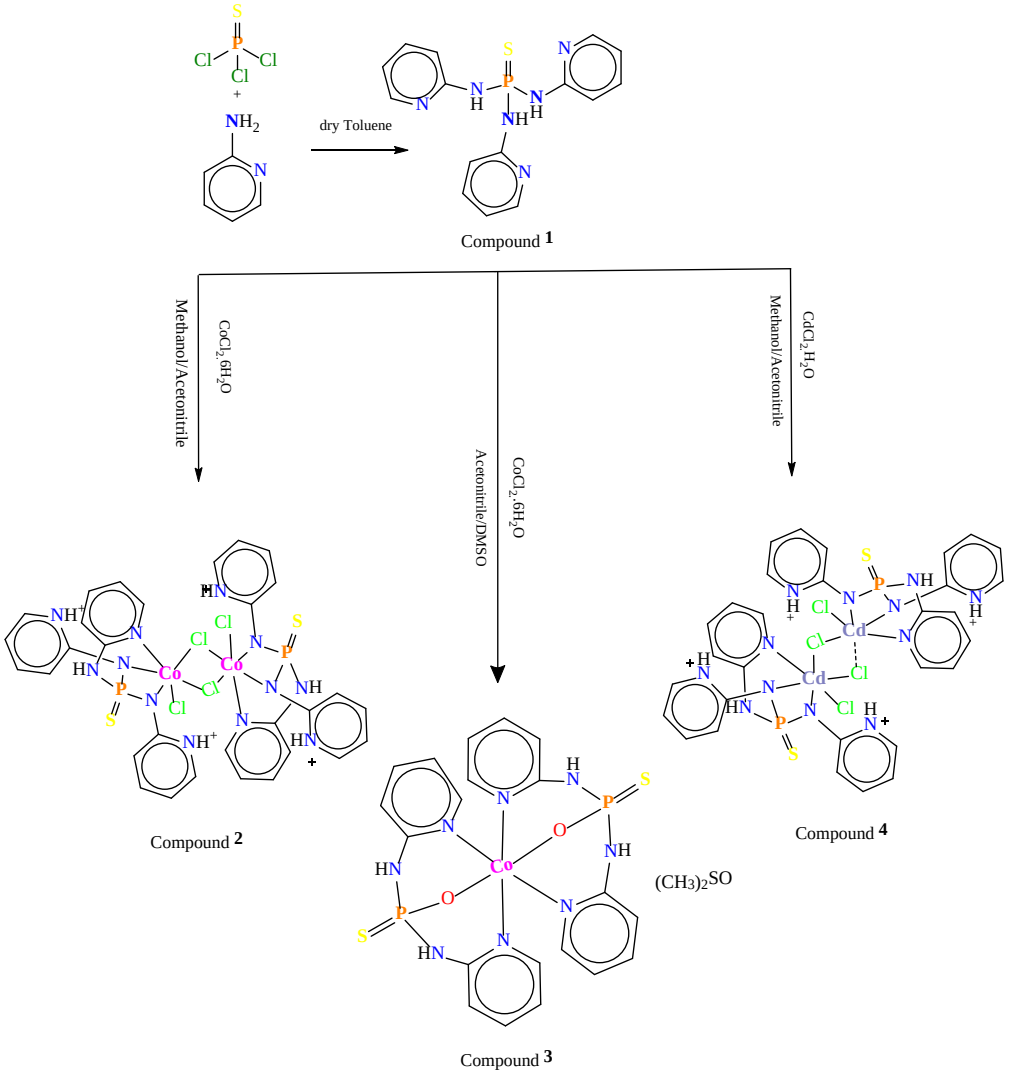

SCHEME 1 Structures and formation reactions of compounds **1** – **4**.

The molecular structures of the studied compounds **1** – **4** are presented in Figs. 1 and 2. The structure of **1** has a tris(pyridin-2-yl)thiophosphoric triamide ligand crystallizing in the monoclinic space group $P2_1/n$ whereas structures **2** – **4** are discrete chelate cobalt(2+) and cadmium(2+) complexes derived from this ligand crystallizing in the monoclinic space group $P2_1/c$ for **2** and **4**, but in the triclinic space group $P\bar{1}$ for **3**. In all these complexes, SPT ligand **1** acts as a trident *N*,*N*,*N*- (for **2** and **4**) or *N*,*N*,*O*-(for **3**) donor ligand, where interestingly the sulfur atom of the P═S thiophosphoryl group does not participate in the coordination to the metal center in all three complexes. The non-participation of the P═S unit in coordination mode can be attributed to the fact that the cobalt(2+) and cadmium(2+) metal ions cannot provide a soft enough coordination response for the P═S motif. The asymmetric unit of **1** is composed of two molecules which are labelled for the following discussion as P3 and P4, while for the binuclear complexes **2** and **4**, the asymmetric unit consists of one-half molecule.

In the case of **3**, one-half molecule complex with the Co^{2+} located on an inversion center along with one dimethyl sulfoxide (DMSO) solvent molecule makes up the asymmetric unit. The DMSO solvent molecule reveals disorder over two positions (with disordered sulfur atom and methyl groups) with major and minor populations of 64% and 36%, respectively.

TABLE 1 Crystal data and structure refinement for compounds **1 – 4.**

Compound	**1**	**2**	**3**	**4**
CCDC number	2174158	2249831	2261634	2261633
Chemical formula	$C_{15}H_{15}N_6PS$	$C_{30}H_{30}Cl_4Co_2N_{12}P_2S_2$	$C_{24}H_{32}CoN_8O_4P_2S_4$	$C_{30}H_{30}Cd_2Cl_4N_{12}P_2S_2$
Moiety formula	$C_{15}H_{15}N_6PS$	$C_{30}H_{30}Cl_4Co_2N_{12}P_2S_2$	$C_{20}H_{20}CoN_8O_2P_2S_2 \cdot 2(C_2H_6OS)$ S4	$C_{30}H_{30}Cd_2Cl_4N_{12}P_2S_2$
M_r (gr/mol)	342.36	944.38	745.69	525.67
Temperature (K)	150	293	293	293
Crystal system, Space group	Monoclinic, $P2_1/n$	Monoclinic, $P2_1/c$	Triclinic, $P\bar{1}$	Monoclinic, $P2_1/c$
a, b, c (Å)	10.5486 (1), 14.0625 (1), 22.2708 (2)	13.7044 (2), 16.0236 (2), 9.2501 (2)	9.0208 (2), 9.5784 (2), 10.8778 (3)	14.1674 (5), 15.9170 (5), 9.1736 (3)
α, β, γ (°)	91.839 (1)	96.563 (1)	100.090 (2), 114.409 (2), 90.454 (2)	95.568 (3)
V (Å^3)	3301.94 (5)	2017.95 (6)	839.26 (4)	2058.91 (12)
Z	8	2	1	2
Radiation type	Cu $K\alpha$	Cu $K\alpha$	Cu $K\alpha$	Cu $K\alpha$
μ (mm^{-1})	2.73	10.93	7.60	12.67
Crystal size (mm)	0.10 × 0.10 × 0.06	0.10 × 0.06 × 0.06	0.20 × 0.20 × 0.20	0.10 × 0.08 × 0.05
Diffractometer	SuperNova, Dual, Cu at home/near, AtlasS2	SuperNova, Dual, Cu at home/near, AtlasS2	SuperNova, Dual, Cu at home/near, AtlasS2	Oxford Diffraction SuperNova
Absorption correction	Multi-scan/*CrysAlis PRO*	Multi-scan/*CrysAlis PRO*	Multi-scan/*CrysAlis PRO*	Multi-scan/*CrysAlis PRO*
T_{min}, T_{max}	0.925, 1.000	0.737, 1.000	0.898, 1.000	0.36, 0.53
No. of measured, independent and observed [$I > 2.0\sigma(I)$] reflections	51456, 6879, 6144	23771, 4257, 3825	19462, 3502, 3455	28409, 4314, 4113
R_{int}	0.046	0.031	0.025	0.030
$(\sin \theta/\lambda)_{max}$ (Å^{-1})	0.629	0.632	0.629	0.630
$R[F^2 > 2\sigma(F^2)]$, $wR(F^2)$, S	0.040, 0.112, 1.00	0.029, 0.077, 0.99	0.039, 0121, 1.00	0.020, 0.049, 0.95
No. of reflections	6879	4257	3502	4314
No. of parameters	439	247	232	248
No. of restraints	24	12	42	12
H-atom treatment	H atoms treated by a mixture of independent and constrained refinement	H atoms treated by a mixture of independent and constrained refinement	H atoms treated by a mixture of independent and constrained refinement	H atoms treated by a mixture of independent and constrained refinement
$\Delta\rho_{max}$, $\Delta\rho_{min}$ (e.Å^{-3})	0.38, −0.25	0.39, –0.27	0.43, –0.38	0.38, -0.50

TABLE 2 Hydrogen bond interactions geometries (Å, °) for compounds **1** – **4**.

D—H···*A*	*D*—H	H···*A*	*D*···*A**	∠*D*—H···*A*
1				
N5—H51···N8	0.85 (2)	2.20 (1)	3.045 (3)	177 (2)
N10—H101···N9	0.84 (2)	2.25 (1)	3.080 (3)	169 (2)
N11—H111···N14	0.85 (2)	2.16 (2)	3.002 (3)	172 (2)
N12—H121···N13	0.85 (2)	2.13 (2)	2.961 (3)	168 (2)
N6—H61···S1^{i}	0.85 (2)	2.61 (2)	3.447 (1)	166 (2)
N7—H71···S2^{i}	0.83 (2)	2.67 (2)	3.453 (1)	158 (2)
2				
N10—H101···Cl3	0.83 (2)	2.55 (2)	3.193 (2)	136 (2)
N11—H111···Cl3^{i}	0.87 (2)	2.42 (2)	3.139 (2)	140 (2)
N8—H81···S4^{i}	0.84 (2)	2.64 (2)	3.418 (2)	154 (2)
3				
N9—H91···O24	0.83 (3)	2.13 (3)	2.951 (6)	168 (2)
N8—H81···S3^{i}	0.83 (3)	2.63 (3)	3.420 (3)	160 (2)
4				
N10—H101···Cl3	0.84 (2)	2.68 (2)	3.358 (2)	139 (2)
N11—H111···Cl3^{i}	0.85 (2)	2.63 (2)	3.290 (2)	135 (2)
N8—H81···S4^{i}	0.84 (2)	2.67 (2)	3.435 (2)	152 (2)

Symmetry transformations used to generate equivalent atoms for **1**: (i) $-x+\frac{3}{2}, y-\frac{1}{2}, -z+\frac{3}{2}$; for **2**: (i) $-x+1, -y+1, -z+1$; (ii) $-x+2, -y+1, -z+1$; for **3**: (i) $-x+1, -y+1, -z$; for **4**: (i) $-x+1, -y+1, -z+1$; (ii) $-x, -y+1, -z+1$.

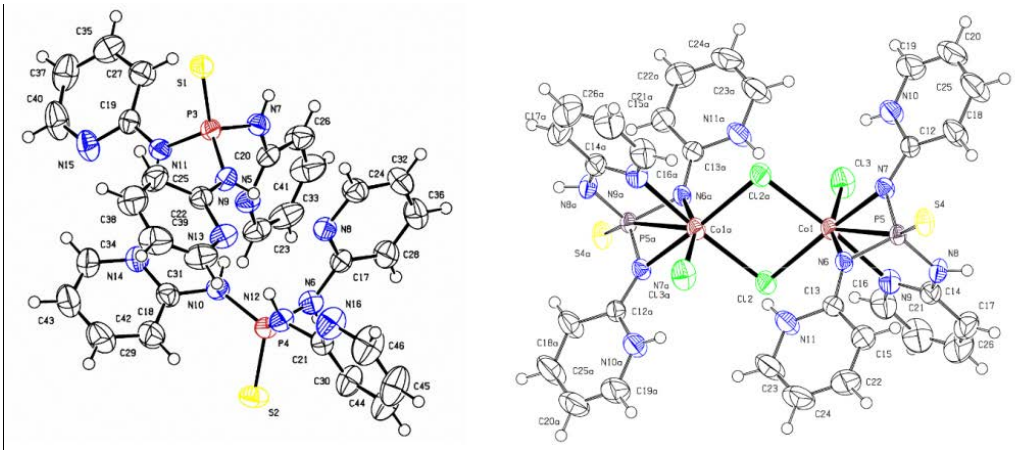

FIGURE 1 Molecular structures of ligand **1** (left) and Co^{2+} complex **2** (right) with 50% displacement ellipsoids. For **1**, the content of the asymmetric unit including two independent molecules P3 and P4 has been shown. H atoms are drawn as circles of arbitrary radii.

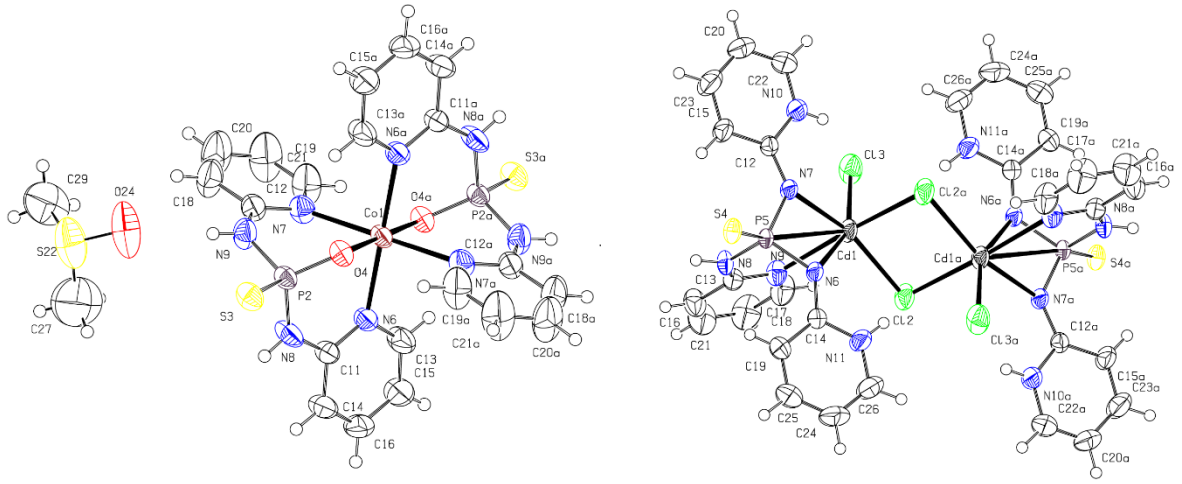

FIGURE 2 Molecular structure of the Co^{2+} and Cd^{2+} complexes of **3** (left) and **4** (right), showing the atom-numbering scheme and displacement ellipsoids at the 50% probability level. H atoms are shown as spheres of arbitrary radius. The disorder of the DMSO solvent molecule for **3** has been omitted for clarity.

For all structures **1** – **4**, the P atom is in a distorted tetrahedral S═P[N]$_3$ environment formed by three nitrogen atoms of amide substitutes and a terminal sulfur atom (Table S1)[30]. However, for the complex **3** containing the amidothiophosphate ligand, this distorted tetrahedral environment for the phosphorus atom is made up by a sulfur, two amido nitrogen and a negative oxygen as S═P[N]$_2$[O$^-$]. In all compounds, the P–N bond lengths and S–P–N and N–P–N angles (Table S1) are in the range of those reported for similar compounds[4c, 31]. The observed P═S bond lengths are in the range of those found in previously reported similar compounds [29] for ligand **1** (1.9411 (5) and 1.9428 (6) Å) and for complex **3** (1.9464 (8) Å) have, but for the metal complexes **2** and **4**, the uncoordinated P=S bonds (1.9568 (6) Å for **2** and 1.9608 (5) Å for **4**) fall out of the range (smaller than 1.96 Å) reported for similar compounds[29]. However, for some similar complexes in which the P=S group coordinates to a metal center a long P=S bond is reported, as in the Cd^{2+} thiophosphoric triamide complex ($CdCl_2$[(S)P(NC_4H_8)$_3$]$_2$, OBUCEX)[32] where the P=S bond lengths are 2.005 (1) and 1.9996 (9) Å. The anomalously long P=S bonds reported here for complexes **2** and **4** may be attributed to the presence of the P—N$^-$ bonds (with negative nitrogen) coordinated to the metal center which may weaken the P=S bond. Indeed, **2** and **4** having a S═P[N$^-$]$_2$[N] segment are the first examples of thiophosphoric triamide complexes in which two P—N$^-$ bond lengths are smaller than P—N bonds in the free ligand and another P—N bond is longer, whereas both P—N bonds of complex **3** having a S═P[N]$_2$[O] segment are longer

than those in the free ligand. Moreover, a comparison of the P═S bonds in the free ligand (compound **1**) and the related complexes **2** – **4** shows that these bonds are slightly longer in complexes than those in the free ligand (Table S1).

Interestingly, the different structures of the Co^{2+} complexes **2** and **3** (Figs. 1 and 2) were obtained from similar reactions between the (S)P[NH-^{2}Py]$_3$ ligand and $CoCl_2.6H_2O$ in a solution of methanol/acetonitrile under reflux condition. Compound **2** is a centrosymmetric binuclear neutral complex containing two tridentate *N*,*N*,*N*-donor thiophosphoric triamide (S)P[NH-^{2}Py]$_3$ ligands in which two units of {(S)P[NH-^{2}Py]$_3$}CoCl are bridged together *via* two chloro ligands (μ_2-Cl) forming a central Co_2Cl_2 core which features a four-membered ring, while compound **3** is a mononuclear complex containing a tridentate *N*,*N*,*O*-donor amidothiophosphate (S)P[O][NH-^{2}Py]$_2^-$ ligand. Indeed, the complex **3** is derived from *in situ* generated pyridyl-functionalized amidothiophosphate ligand attributed to the low Lewis acidic nature of the Co^{2+} salt which leads to a metal-assisted P–N bond hydrolysis at the same point in the reaction[33]. Such an amidothiophosphate complex with an $Co(N)_4(O)_2$ environment has not yet been reported up to now[29]. Moreover, based on a CSD survey the compounds **2** and **4** appear to be the first binuclear complexes of a SPT ligand with an $M(N)_3(Cl)_3$ (M = Co and Cd) environment.

For both complexes **2** and **3**, the Co^{2+} cation features a hexa-coordinate environment $Co(N)_3(Cl)_3$ (for **2**) / $Co(N)_4(O)_2$ (for **3**) adopting a distorted octahedral geometry. However, in the case of **2**, the octahedral structure for each of Co^{2+} is slightly deformed which may be depicted as a pseudo-octahedral geometry. This slight distortion from the ideal octahedral geometry can be attributed to the presence of the chelating tridentate thiophosphoramide ligand and the steric constraints imposed by it, as is found also for similar chelate complex structures[34].

In **2**, for each cobalt center, three coordinating nitrogens (one pyridine nitrogen (N_{Py}) and two negative nitrogens (N^-)) are provided by the chelating *N*,*N*,*N*-donor SPT (S)P[NH-^{2}Py]$_3$ ligand. Indeed, in each neutral SPT ligand the two pyridine nitrogen atoms which are not coordinated to the metallic centre are protonated as NH^+ and the two NH groups connected to this pyridine rings are deprotonated as N^-, thus providing charge balance. The six-coordinate environment is completed by three chlorines (two bridged and one terminal Cl), where the N and Cl atoms are in the *anti*-positions to each other as shown in Fig. 1. The two positive charges of each cobalt metal are balanced by the negative charges of the chlorine ions. These

bridged chlorine atoms are at almost the same distance to the Co center (2.4379 (5) and 2.4735 (6) Å, Table S1) but they are at a longer distance than the terminal Cl atom (2.4110 (7) Å). In this structure, the Co atom lies about 0.117 Å above the four-membered plane introduced by the two μ_2-Cl and the two N atoms towards the terminal Cl atom. The Co–N^- bond lengths (2.166 (1) and 2.188 (1) Å) are shorter than the Co–N_{Py} bond (2.239 (2) Å) as expected. The *trans* N–Co–Cl angles are 175.76 (5), 168.80 (5) and 160.77 (4)°, and those for *cis* N–Co–N and Cl–Co–Cl angles vary from 67.79 (6) to 88.66 (6)° and from 83.64 (2) to 96.43 (2)°, respectively, forming a distorted octahedral geometry around each central Co^{2+} cation.

For **3**, four of the coordination octahedral sites are occupied by the pyridine nitrogen atoms (N_{Py}) provided by the two chelating *N*,*N*,*O*-coordination amidophosphate ligands and the two remaining coordination sites, *trans* relative to each other, are occupied by two O^- contacts. In this structure, the Co–O distance is 2.0261 (15) Å and the Co–N bonds measure 2.170 (2) Å and 2.252 (2) Å. The *cis* N–Co–O and O–Co–O angles change from 87.75 (7) to 92.25 (7) and those for the *trans* N–Co–N and O–Co–O angles are about 180.0° affirming a disordered octahedral environment around the central Co^{2+} cation.

Complexes **2** and **4** are isostructural; both are centrosymmetric binuclear complexes formed from two (S)P[NH-^{2}Py]$_3$ ligands in which two units of {(S)P[NH-^{2}Py]$_3$}CdCl or {(S)P[NH-^{2}Py]$_3$}CoCl are connected together *via* two bridging chloro ligands (μ_2-Cl) and each Cd^{2+} (Co^{2+}) center adopts a deformed $M(N)_3(Cl)_3$ octahedral environment. The *trans* N–Cd–Cl and *cis* N–Cd–N and Cl–Cd–Cl angles (Table S1) are significantly different from 180° and 90°, respectively, confirming the deformed geometry around the Cd^{2+} center. The thiophosphoric triamide (S)P[NH-^{2}Py]$_3$ ligand acts as a chelating *N*,*N*,*N*-donor ligand providing three coordinated nitrogen atoms. As expected, the bridged Cd—Cl bond lengths are longer than the terminal Cd—Cl bond and all Cd—Cl bonds are larger than the comparable Co—Cl bonds in **2**. The deviation of the Cd center from the plane defined by the two μ_2-Cl and the two N atoms is about 0.260 Å which is larger than that for the Co center in **2**.

An analysis of the hydrogen bonding (H-bonding) assemblies illustrates that in the crystal structure of **1**, classical N—H…N interactions are found between two symmetrically-independent molecules and for **3**, classical N—H…O═S interactions are found between the complex and solvent DMSO molecule (Table 2). Some intramolecular N—H…Cl H-bonding

interactions are found in the structures **2** and **4** (Table 2). Moreover, the uncoordinated thiophosphoryl sulfur atoms are involved in non-classical N—H…S interactions connecting the neighbouring molecules as one-dimensional (1D) linear arrangements along the *b* (for **1**) / *a* (**2** and **4**) / *c* (for **3**) axis (Figs. 3 and 4), where the N—H unit involved in the N—H…S interaction adopts a *syn*-position relative to the P═S group. In the case of **3**, the solvent DMSO molecules are connected to the N—H…S HB chain *via* classical N—H…O═S hydrogen bonding interaction (Table 2, Fig. 4).

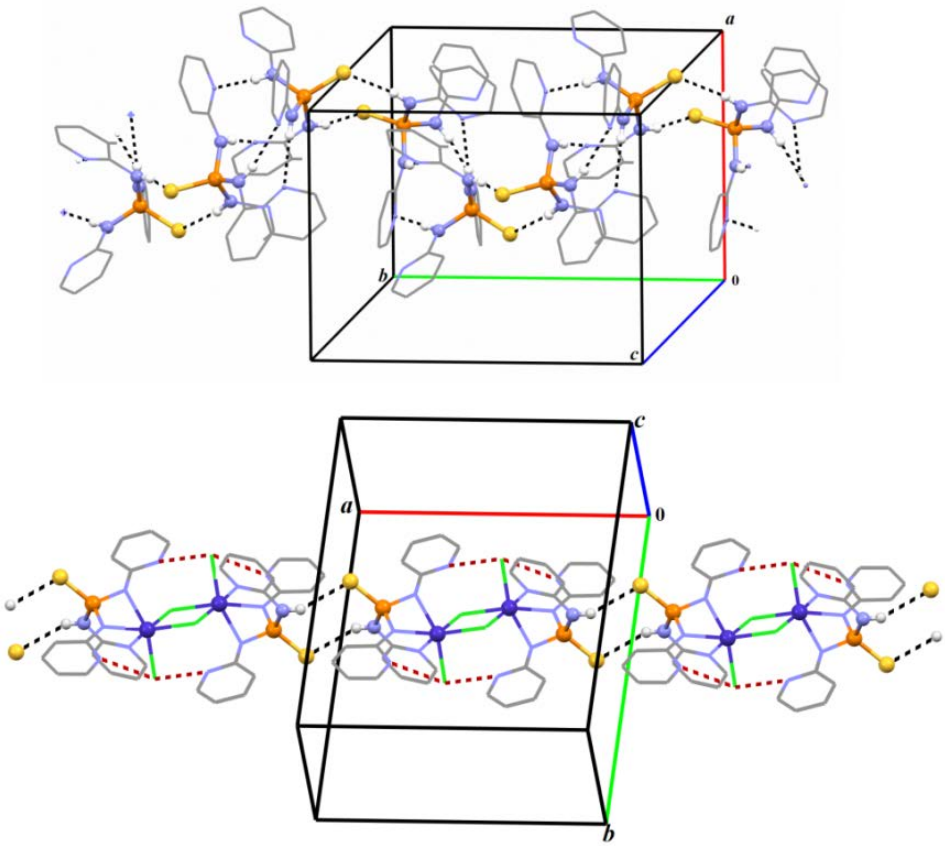

FIGURE 3 Packing network of the structures **1** (up) and **2** (down) showing the 1D linear arrangements produced *via* non-classical hydrogen bonding N—H…S interactions along the *b* (for **1**) and *a* (**2**) axis. The intermolecular N—H…N (in **1**) and N—H…S (in **1** and **2**) interactions are shown as black dashed lines and the intramolecular N—H…Cl interactions are shown as red dashed lines. H atoms not involved in hydrogen bonding interactions have been omitted for clarity. The S═P─NH segments involved in hydrogen bonding and metal atoms are shown as 'ball and sticks'.

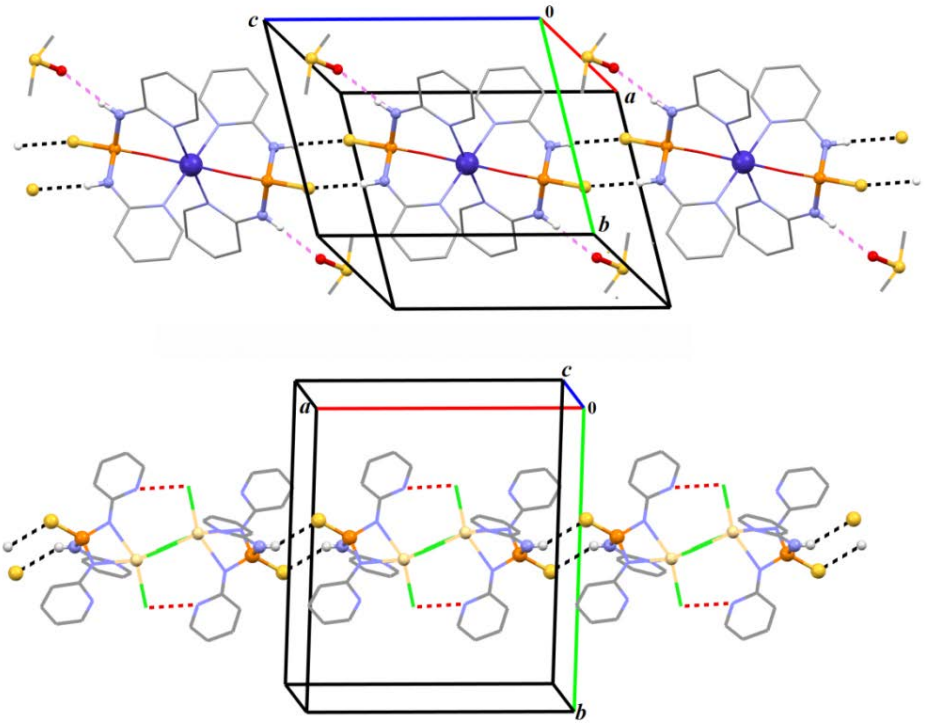

FIGURE. 4 Packing network of the structures **3** (up) and **4** (down) showing the 1D linear arrangement formed *via* the non-classical N—H…S hydrogen bonding interactions (black dashed lines) along the *c* (**3**)/ *a* (**4**) axis. In **3**, the N—H…O═S interactions between the complex with DMSO solvent molecule and in **4** the intramolecular N—H…Cl interactions are shown as violet and red dashed lines, respectively. H atoms not involved in hydrogen bonding interactions have been omitted for clarity. The N—H…O═S (for **3**), S═P─NH (for **4**) segments and metal atoms involved in hydrogen bonding are shown as 'ball and sticks'.

3.3 Hirshfeld surface (HS) analysis and Enrichment ratio (E_{XY})

The relative contributions of intermolecular contacts and the calculated enrichment ratios (E_{XY}) resulting from the Hirshfeld surface analysis are presented in Table S2. Data visualization as 3D d_{norm} Hirshfeld surfaces (HSs) and 2D full fingerprint plots (FPs) are shown in Figures 5, S1 and S2. It should be noted that for **3**, two HS analyses were separately performed for this structure with each of the minor and major disordered components of the DMSO solvent molecule. The two analyses led to very similar interaction results, and therefore, only major component was further analyzed as being fully occupied.

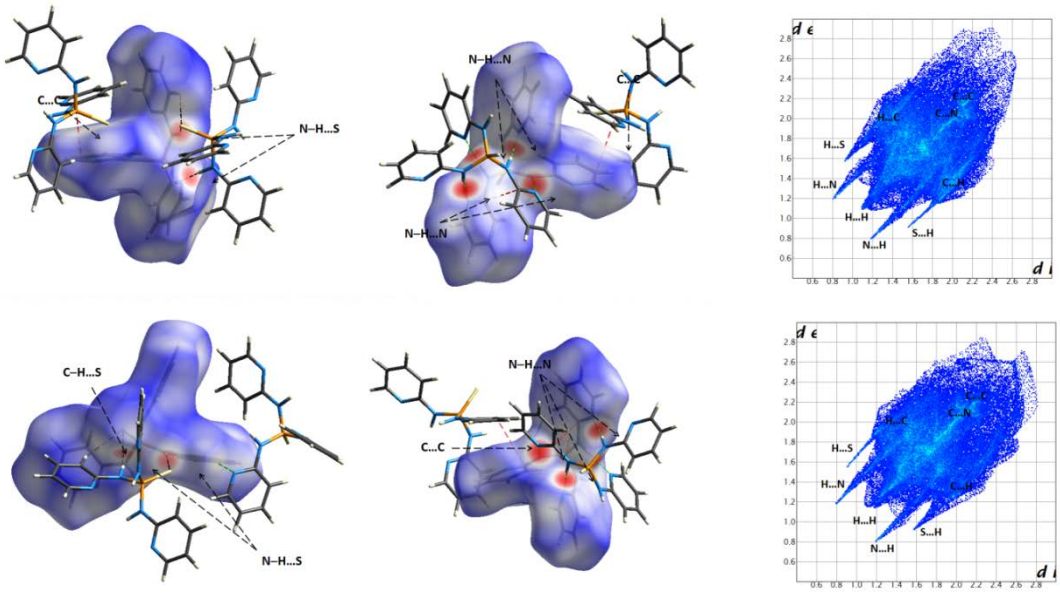

FIGURE 5 Left and middle: Hirshfeld surface mapped with d_{norm} for the molecules P3 (up) and P4 (down) of **1** showing intermolecular short contact interactions appeared as red spots; Right: Full fingerprint plots of the molecules P3 (up) and P4 (down) of **1** showing important intermolecular interactions.

In Figure 5, the red hot spots in the d_{norm} HS of the molecules P3 and P4 of **1** are related to the N—H…N interactions, whereas the slightly light red ones refer to the N—H…S interactions (Table 2). For complexes **2** and **4**, the relatively small red spots on the d_{norm} surface result from N—H…S and C—H…Cl interactions (Fig. S1 and Table 2) and the tiny red ones on the white areas are related to the C—H…S interactions (Table 2). In the complex **3**, the respective acceptor and donor atoms presenting the N—H…O hydrogen bond interaction between the complex and solvent molecules and the N—H…S between two complex molecules (Table 2) are indicated as large red spots on the Hirshfeld surface (Fig. S2). Some little light red spots also appear on the d_{norm} HS of **3** featuring the C—H…O and C—H…S contacts.

From the FPs which give the percentage of various intermolecular interactions contributed to HS (Figs. S3 – S7), it is concluded that the highest contribution of contacts to the HS is found for the H…H contacts for all compounds with a percentage of around 45% for **1** and **3** and around 38% for **2** and **4**. This result is can be attributed to the abundance of hydrogen atoms on the molecular surfaces, although these H…H contacts do not play any important role in the stabilization of structures. The shortest H…H contacts are displayed as a spike on the diameter plot with lowest values of $d_e + d_i \approx 2.2$ Å. The H…C/C…H,

H…S/S…H and H…N/N…H contacts are the next most frequent interactions. Moreover, the H…Cl/Cl…H contacts are only found in the complexes **2** and **4** and the H…O/O…H contacts are special for the complex **3**.

For both molecules of **1**, the shortest contacts are related to the close H…N/N…H contacts covering classical N—H…N hydrogen bonds. These H…N/N…H contacts appear as a pair of sharp spikes located on both sides of the diameter plot with a $d_e + d_i$ sum of 2.0 Å. Another pair of sharp spikes with a minimum value of $d_e + d_i \approx 2.5$ Å is also observed on the FPs of **1** attributed to the H…S/S…H contacts which is in agreement with the presence of the N—H…S interactions.

In complexes **2** and **4**, three pairs of spikes are found in the FP which are related to the H…S/S…H interactions (with a minimum value of $d_e + d_i \approx 2.5$ Å, 13.0% for **2** and 12.3% for **4**), H…Cl/Cl…H ($d_e + d_i \geq 2.6$ Å, 13.3% / 15.0%) and H…N/N…H ($d_e + d_i \geq 2.7$ Å, 7.6% / 8.4%) contacts, where the H…Cl/Cl…H spike is located between the H…S/S…H and H…N/N…H spikes.

In the case of **3**, the FP is asymmetric as a consequence of the presence of more than one component (two complex and solvent molecules) in the crystal structure. A sharp spike associated with the H…S contacts with a minimum value of $d_e + d_i \approx 2.5$ Å appears in the upper left part of the plot, while the S…H contacts lead to two sharp spikes next to each other ($d_e + d_i \geq 2.5$ Å and 2.8 Å) pointing towards the bottom right part of the plot. Another sharp spike in the bottom left part of the plot with a minimum value of $d_e + d_i \approx 2.0$ Å is associated to the H…O contacts, whereas other O…H contacts are scattered on the right side of plot.

C…C and C…N/N…C contacts are visible in the FPs in the range of 1.6 Å < d_e , d_i < 2.6 Å in **1**, 1.8 Å < d_e , d_i < 3.0 Å in **2** and **4** and 2.0 Å < d_e , d_i < 2.4 Å in **3** for C…C and 1.6 Å < d_e , d_i < 2.2 Å in **1**, 1.8 Å < d_e , d_i < 3.0 Å in **2** and **4** and 2.0 Å < d_e , d_i < 2.3 Å in **3** for C…N/N…C.

The enrichment ratios listed in Table S2 highlight that H…S/S…H ($1.43 \leq E_{HS} \leq 1.59$) and H…N/N…H ($1.19 \leq E_{HN} \leq 1.27$) contacts are favored for all studied structures. However, the C…C contacts which support π…π stacking interactions dominate all contacts in all structures **1** – **4** and are very favored with $E_{CC} > 2.0$. The H…Cl/Cl…H (for **2** ($E_{HCl} = 1.55$) and **4** (1.58)) and H…O/O…H ($E_{HO} = 1.51$ for **3**) contacts are enriched. The behavior of

H…C/C…H contacts in **1** – **4** is different as E_{HC} tends towards a value close to unity for **3** with E_{HC} = 1.08, whereas H…C/C…H for other compounds is found to decrease below unity with values around 0.8. In the case of the H…H contacts, E_{HH} ratios are less than unity with values around 0.9 for **1**, **2** and **4**, while the H…H contacts in **3** tend to be enriched and E_{HH} reaches to unity with a magnitude of 1.05. The C…N/N…C contacts are impoverished for ligand **1** with E_{CN} = 0.8, where S_N is nearly large and the N atoms are involved in the classical N—H...N hydrogen bond interactions. For the complexes **2** – **4**, the C…N/N…C contacts turn out to be favored and E_{CN} tends towards values larger than unity (Table S2), where the N atoms are coordinated to metal center or are involved in the non-classical N—H...S hydrogen bonds.

3.4. Biological essays

3.4.1. Assessment of cytotoxicity using MTT assay

Treatment of breast cancer with suitable drugs such as Glufosfamide belong to phosphoramide mustard family[35] plays an important role in reducing the number of breast cancer victims. Here, the antiproliferative effect of the studied compounds **1** – **4** were studied against MDA-MB-231 cell lines (breast cancer) by MTT assay using various concentrations (12.5, 25, 50, 75, and 100 nmol) of each compound for 72 h. After having reached the quorum of the number of cancer cells cultured in 1640 RPMI medium containing 10% Fetal Bovine Serum (i.e. when the percentage of viable cells was greater than 90%), the cells were treated at the mentioned concentrations. As can be seen in Figure 6, the survival percentage of cancer cells decreases drastically with the increase of the concentration of the synthesized compounds.

Moreover, a comparison of the antiproliferative activity of the studied compounds with the control group (containing culture medium and cancer cells) shows that the compounds are more effective against MDA-MB-231 cells than the title control group. After the treatment of the synthesized compounds with a concentration of 250 µl, the greatest reduction in the survival rate of cancer cells was observed.

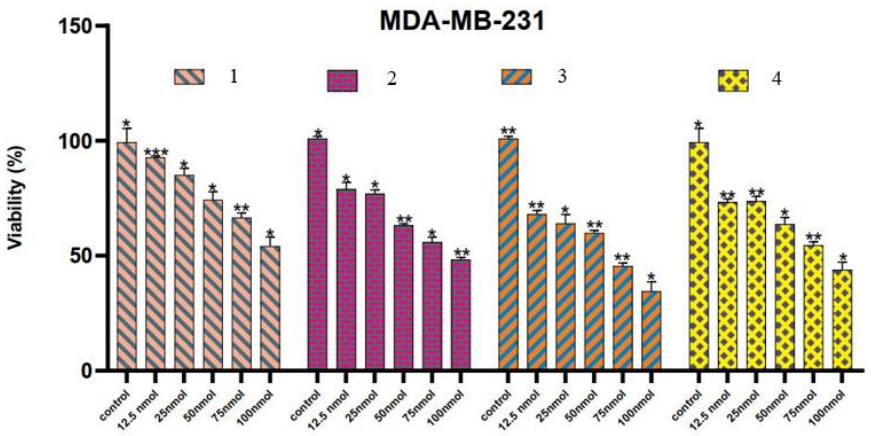

Figure 6 Diagram of cell viability percentage versus different concentrations of treatment agents obtained from MTT assay results. Asterisks on each column describe P-value (Probability value which is indicative of statistical significant of results in comparison with control sample), where P values less than 0.001 ($P \leq 0.001$) are shown as three asterisks, and those less than 0.01 ($P \leq 0.01$) and 0.05 ($P \leq 0.05$) are displayed as two and one asterisks, respectively.

The IC50 values of the synthesized ligand and complexes are presented in Table 3. Based on these values, it can be concluded that complex **3** shows a good activity with an IC50 value of 62 nM which is comparable to that of 5-Fluorouracil (a cytotoxic chemotherapy drug used to treat cancer which was employed as a control drug in this project). By intravenous injection, it is used to treat various cancers, such as colon, esophageal, stomach, pancreatic, breast, and cervical cancers. Cells treated with ligand **1** and complexes **2** and **4** display a weak antiproliferative effect with IC50 values of 112, 82 and 85 nM at 48 h, respectively.

TABLE 3 Inhibitory concentration (IC50, nM) of studied compounds **1** – **4** and the standard drug.

IC50 (nmolar) of compounds in MDA-MB-231				
1	**2**	**3**	**4**	**5-FU**
112.0 ± 1.7	81.9 ± 3.2	62.0 ± 1.4	84.7 ± 2.2	29.3 ± 1.8

3.4.2. Spectrophotometric determination of DPPH radical scavenging activity

Antioxidant capacity analysis using the DPPH radical method is a well-known test to measure the antioxidant power of various compounds. The basis of this method is to reduce the numbers of DPPH free radicals by using antioxidants in the absence of other free radicals.

The obtained result is generally compared to that of a known antioxidant compound such as vitamin C. In this work, the ability of the synthesized compounds **1** – **4** to inhibit DPPH was tested at concentrations of 3.0, 7.81, 15.62 and 31.25 µg mL $^{-1}$, respectively and the results are shown in Figure 7. The calculated EC_{50} values are given in Table 4. The results show that in all investigated concentrations, ascorbic acid (control drug) has a more radical scavenging activity compared to the compounds of this study. The maximum of DPPH radical scavenging activity in **1** – **4** is for the Cd^{2+} complex **4** (70% in the presence of 125 µg mL^{-1} of **4** and EC_{50} = 68.1 ± 2.6). The free ligand **1** displays a higher antioxidant activity compared to the Co^{2+} complexes of **2** and **3** derived from it.

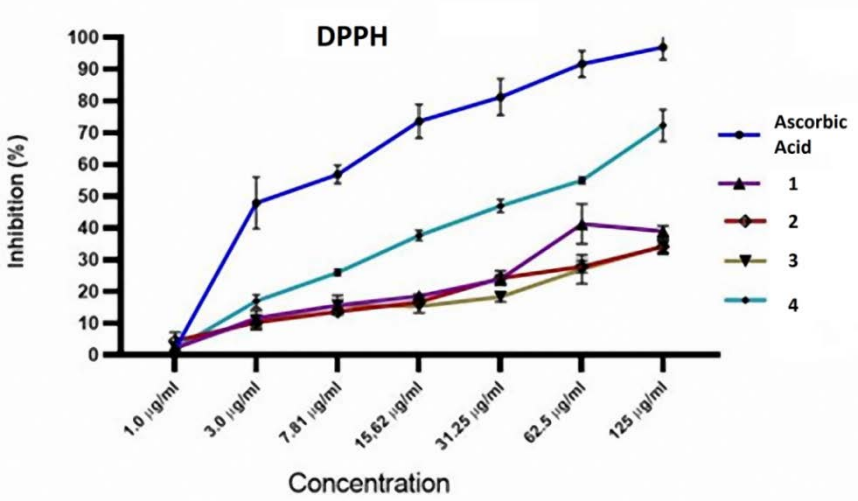

FIGURE 7 Scavenging effect of the studied compounds **1** – **4** on DPPH radical at various concentrations.

Table 4 Radical scavenging activity of DPPH ligand and the studied compounds **1** – **4**.

Compound	**1**	**2**	**3**	**4**	Ascorbic Acid
EC_{50} (µg mL^{-1})	185.1± 1.02	232.5± 0.56	220.7± 3.43	68.1± 2.6	4.2± 0.23

3.4.3. Hemolysis activity

The anti-hemolytic activity of the current thiophosphoramide compounds was investigated in blood samples. The hemolytic activity percentage versus concentration is shown in Fig. 8. All compounds show significant hemocompatibility as a drug delivery application. As seen in figure 8, the compounds exhibit an increase in anti-hemolytic activity with increasing concentration. However, an exception is found in the case of ligand **1**, where the anti-hemolytic activity of **1** is found to decrease at higher concentration of 125 µg/mL. The Cd^{2+} complex **4** illustrates a better anti-hemolytic activity than the other compounds.

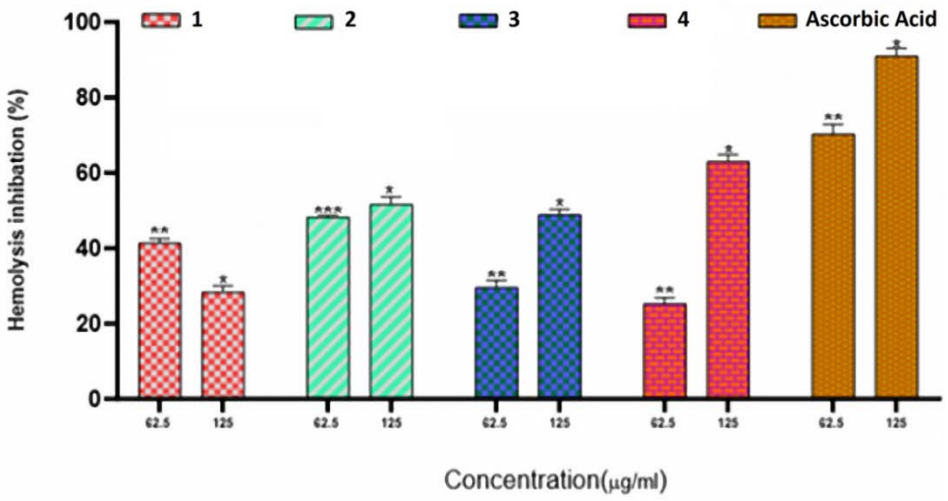

FIGURE 8 Graphical representation of % hemolysis inhibition of **1** – **4** at two concentrations of 62.5 and 125 µg/mL. Asterisks on each column describe P-value (Probability value which is indicative of statistical significant of results in comparison with control sample), where P values less than 0.001 ($P \leq 0.001$) are shown as three asterisks, and those less than 0.01 ($P \leq 0.01$) and 0.05 ($P \leq 0.05$) are displayed as two and one asterisks, respectively.

3.5. Molecular docking study

Docking is a molecular modeling technique to predict the binding modes of a compound with various biological molecules/targets via non-covalent interactions. We evaluate here the inhibitory potential of the synthesized compounds against three biological targets of DNA, SARS-CoV-2 and Monkeypox. In all docking simulations, the best position of ligand with target receptor showing the highest negative binding affinity was selected and analyzed. The molecular docking results reported in terms of binding energy (kcal/mole) for the compounds **1** – **4** are listed in Tables 5, 6 and 7.

3.5.1. Molecular docking with DNA as receptor (PDB IDs: 1BNA and 4FM9)

In the context of breast cancer, the nature of binding of the synthesized compounds is simulated against the 1BNA dodecamer and 4FM9 breast cancer receptor. The binding affinities for all four studied compounds are negative (–7.79 kcal/mol (for 1BNA) / –8.29 kcal/mol (for 4FM9), –5.67 / –5.81), –7.81 / –7.60 and –6.94 / –7.57 kcal/mol) which are comparable to reported binding energies of investigated bioactive complexes[36] confirming the disturbing effect of the studied compounds on the activity of the target protein (Table 7). However, the thiophosphoric triamide ligand **1** and the Co^{2+} complex **3** derived from it have

slightly larger negative binding affinities (around –8 kcal/mol) illustrating a greater tendency to bind to DNA compared to the complexes **2** and **4** (around –6/–7 kcal/mol). Moreover, the binding values are close to those of some anti-cancer drugs such as Gemcitabine (with the inhibitory potential of –6.5 kcal/mol to the target protein 1BNA), Temozolomide (–7.6 kcal/mol/1BNA)[37] and Etoposide (–8.4 kcal/mol/4FM9)[38]; so, **1** – **4** can be suggested as compounds with a good anti-cancer potential.

TABLE 5 Affinity energies (kcal/mol) and molecular docking interactions between the biological DNA targets 1BNA and 4FM9 with compounds **1** – **4** (ligands).

Receptor	Ligand	Affinity energy	Interaction	Interacted amino acid residue
DNA				
1BNA				
	1	–7.79	van der Waals	DC B:15, DG B:14, DG A:12, DC A:9, DT B:19, DA B:18
			Conventional hydrogen bond	DG B:16, DA B:17, DC A:11, DG A:10
			π-sulfur	DG B:16
	2	–5.67	van der Waals	DC A:11, DG A:10
			Conventional hydrogen bond	DG A:12, DG B:16
			Attractive charge	DG B:16
			Unfavorable negative-negative	DG B:16
			Carbon hydrogen bond	DG B:16, DC B:15, DG B:14
			π-Alkyl	DG B:14
	3	–7.81	van der Waals	DG A:4, DC B:23, DG B:22, DT A:7
			Conventional hydrogen bond	DC B:21
			π-Anion	DA A:6
			π-sulfur	DA A:5
	4	–6.94	van der Waals	DG A:4,DA A:5, DT B:20
			Attractive charge	DC B:23, DT A:8, DT A:7
			Unfavorable negative-negative	DG B:22
			π-Alkyl	DA A:6
			π-sigma	DC B:21
4FM9				
	1	–8.29	van der Waals	VAL A:869, PHE A:895, GLY A:897, ASN A:894, ASN A:780, ILE A:899, PHE A:867, LYS A:1186
			Conventional hydrogen bond	TYR A:892, SER A:891
			π-Anion	ASP A:868
			π-Alkyl	LYS A:893
	2	–5.81	van der Waals	LEU A:829, HIS A:824, ASP A:823, LYS A:827, TYR A:1029, THR A:825, LEU A:1032, GLU A:1035, GLU A:1092
			Conventional hydrogen bond	LEU A:826, PHE A:828, TYR A:830
			Unfavorable positive-positive	ARG A:835
			π-Alkyl	TRP A:1036
	3	–7.60	van der Waals	LYS A:1091, HIS A:824, ASP A:823, THR A:825, LEU A:826, LYS A:827
			Conventional hydrogen bond	TRP A:1090, GLU A:1092, TYR A:830, PHE A:828
			Unfavorable positive-positive	ARG A:835
			π-sulfur	TPR A:1036
	4	–7.57	van der Waals	LYS A:827, TYR A:830, ASP A:831, ASN A:833, PHE A:828, LYS A:599, PRO A:681, PRO A:593
			Conventional hydrogen bond	GLU A:596

	Attractive charge	GLU A:682
	π-Alkyl	LEU A:829, LYS A:676, ARG A:672

Figures 9 and S8 – S13 show the various interactions between 1BNA and 4FM9 and the synthesized compounds. In the case of 1BNA, the most important interactions for **1** are found between the amino acid residues DG B:16, DC A:11 and DG A:10 with the P═S group, and between DG B:16 and DA B:17 with the N–H unit. For the target protein 4FM9 (Figs. 9, S12 and S13), the interactions between the P═S group with the amino acid residues ASN A:894 and ASP A:868, the N–H units with TYR A:892 and SER A:891, and the aromatic rings with ASP A:868 and LYS A:893 are the most important interactions for **1**. The various interactions between the target proteins 1BNA and 4FM9 with the studied compounds are presented in Table 5.

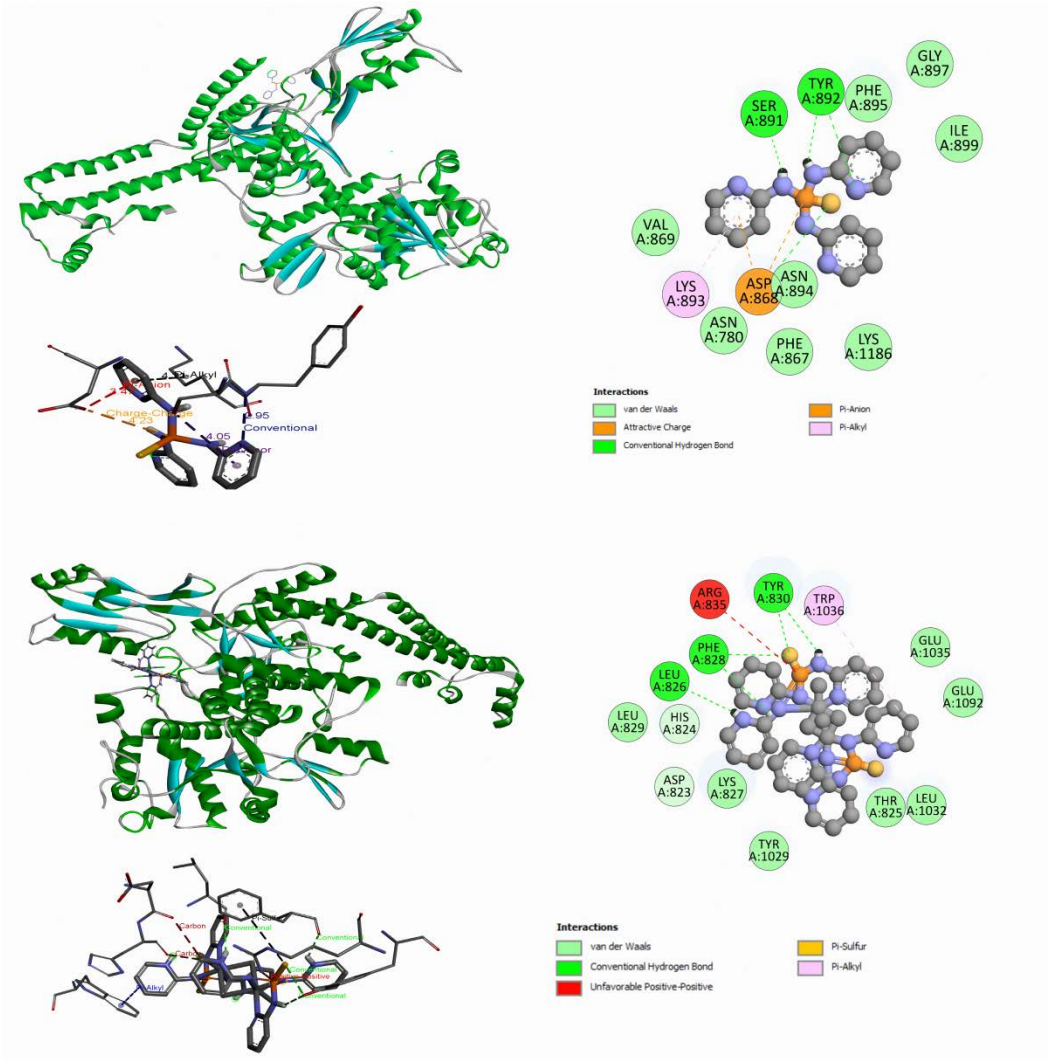

FIGURE 9 Visual description of the 2D and 3D representation maps of the compounds **1** (up) and **2** (down) in the best position relative to 4FM9 showing the highest negative binding affinity.

3.5.2 Molecular docking with SARS-CoV-2 as receptor (PDB IDs: 6LU7 and 6M03)

In this section, the molecular docking method is used to investigate the affinity binding of the studied compounds **1** – **4** with the receptor proteins 6LU7 and 6M03 of SARS-CoV-2. The molecular docking table and figures are shown in Table 6 and Figures 10 and S14 – S19.

The values of binding energies are calculated as –7.79 kcal/mol (for 6LU7) / –7.97 kcal/mol (for 6M03), –5.51 / –6.35), –7.54 / –8.59 and –7.56 / –8.89 kcal/mol, respectively, for the compounds **1** – **4**. Based on these negative energy values, the binding interaction of the studied compounds to the receptor is evident. In the case of 6LU7, the more negative relative binding energy of ligand **1** suggests more ability to bind to the receptor than the other compounds, while for 6M03, it is rather the Cd^{2+} complex **4** which has the largest inhibitory effect. The here reported binding energies are comparable to those of investigated bioactive complexes[39]. Moreover, a comparison of the these binding energies with those of coronavirus drugs such as Remdesivir (–7.2/–7.8 kcal/mol with respect to the target proteins 6LU7/6M03), Chloroquine (–5.4/–6.5 kcal/mol) and Hydroxychloroquine (–5.6/–6.1 kcal/mol)[40] show that they are rather similar, suggesting that **1** – **4** are also potential inhibitors to for the coronavirous.

For the target protein 6LU7 (Figs. 10, S14 and S15), the most important interactions are observed between the amino acid residue GLN A:189 with the P═S group, HIS A:41 and MET A:49 with the aromatic rings, and CYS A:145, HIS A:164 and MET A:165 with the N–H units for **1**. For the target protein 6M03 (Figs. S16 – S19), the interactions between the P═S group with the amino acid residues GLY A:120 and GLU A:14, the aromatic rings with ALA A:70, LYS A:97 and GLU A:14, and the N–H unit with MET A:17 for **1** are obvious. The details of various interactions between the studied compounds with the target proteins 6LU7 and 6M03 are summarized in Table 6.

TABLE 6 Affinity energies (kcal/mol) and molecular docking interactions between the biological SARS-CoV-2 targets (6LU7 and 6M03) with compounds **1** – **4** (ligands).

Receptor	Ligand	Affinity energy	Interaction	Interacted amino acid residue
SARS-CoV-2				
6LU7	**1**	–7.82	van der Waals	HIS A:172, HIS A:163, PHE A:140, SER A:144, ASN A:142, GLU A:166, GLY A:143, LEU A:27, LEU A:141, MET A:165, THR A:25, ASP A:187, TYR A:54, ARG A:188
			Conventional hydrogen bond	CYS A:145, GLN A:189, HIS A:164
			π-sulfur	MET A:49
			π-π stacked	HIS A:41
	2	–7.54	van der Waals	THR A:190, ARG A:188, GLN A:192
			Conventional hydrogen bond	GLU A:166, GLN A:189
			Alkyl, π-Alkyl	ALA A:191, LEU A:50, LEU A:167, MET A:165, PR A:168
	3	–5.51	van der Waals	GLN A:107, ILE A:106, CYS A:160, VAL A:104, LYS A:102, THR A:111, ILE A:152, THR A:292, GLN A:110
			Conventional hydrogen bond	ASN A:151, SER A:158
			π-cation/anion	ASP A:153, PHE A:294
	4	–7.56	van der Waals	GLN A:192, ARG A:188, THR A:190
			Conventional hydrogen bond	GLN A:189, GLU A:166
			Alkyl, π-Alkyl	MET A:165, LEU A:167, ALA A:191
			π-sigma	PRO A:168
6M03				
	1	–7.97	van der Waals	PRO A:122, GLY A:71, GLY A:15, GLN A:19, VAL A:18, SER A:121, ASN A:119, TRP A:31, ASN A:95, CYS A:16, GLN A:69
			Conventional hydrogen bond	GLY A:120, MET A:17, LYS A:97, GLU A:14
			π-sigma	ALA A:70
	2	–8.59	van der Waals	ARG A:298, ASP A:295, TYR A:154, THR A:292, THR A:111, GLN A:110, ASN A:151, ILE A:106, ILE A:152, CYS A:156, SER A:158, PHE A:8, PROA:252
			Alkyl, π-Alkyl	VAL A:303, PHE A:305, VAL A:297, PHE A:294
			Unfavorable negative-negative	ASP A:153
	3	–5.50	van der Waals	SER A:284, ALA A:285, LYS A:5
			Unfavorable bump	LEU A:286
			Salt bridge	GLU A:288
	4	–8.89	van der Waals	GLN A:306, GLY A:11, GLY A:15, ASN A:95, PRO A:99, PRO A:96, ASP A:155
			Conventional hydrogen bond	THR A:98

	Alkyl, π-Alkyl	LYS A:97, LYS A:100
	Attractive charge	LYS A:12

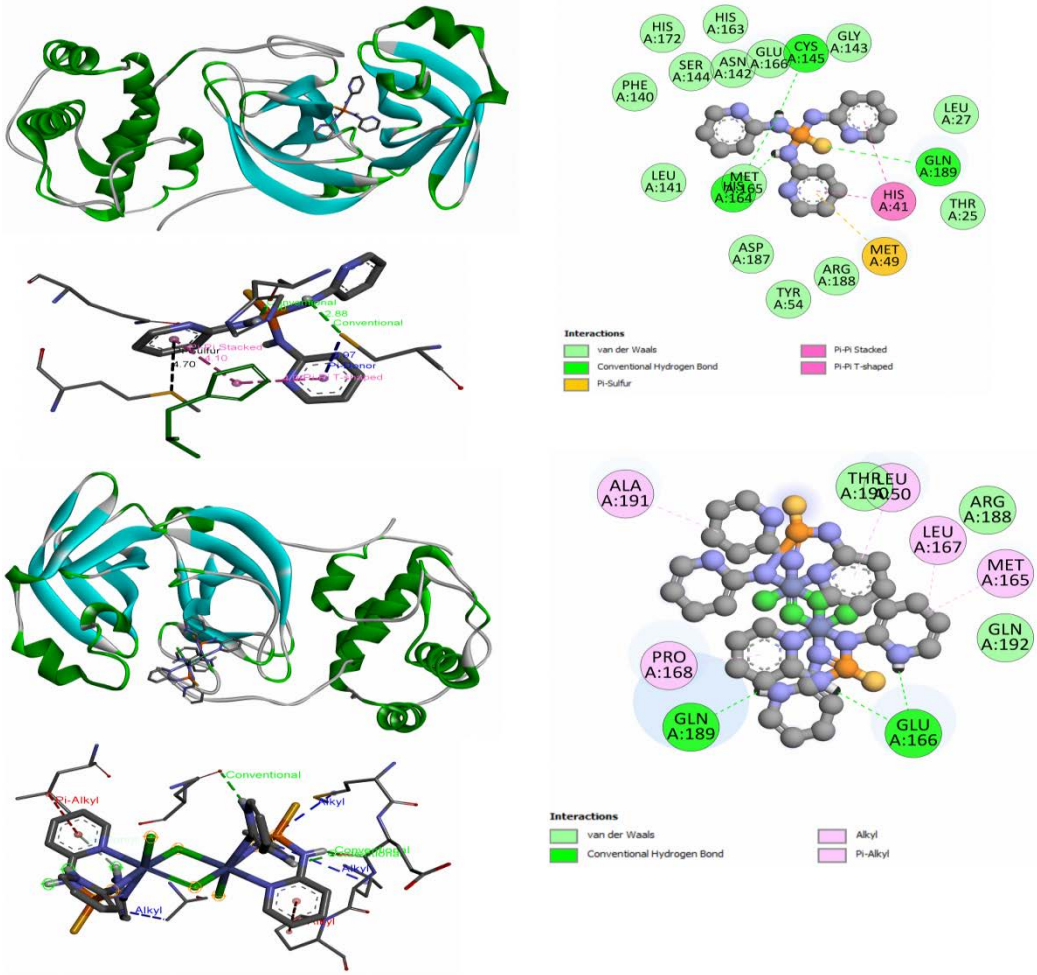

FIGURE 10 Visual description of the 2D and 3D representation maps of the compound **1** (up) and **2** (down) in the best position relative to 6LU7 showing the highest negative binding affinity.

3.5.3 Molecular docking of Monkeypox (Mpox) virus (PDB IDs: 4QWO and 8CER)

Monkeypox is a viral disease which is observed mostly in central and western Africa but much less frequently in the U.S.A. and Europe. The monkeypox virus is related to that which causes smallpox; both viruses have almost similar clinical features[41]. In order to treat this virus, smallpox vaccination with a reported protection of around 85% and antiviral agents such as Brincidofovir and Tecovirimat in the case of high-risk patients are recommended[42].

The molecular docking table and figures for the current compounds **1** – **4** against target proteins 4QWO and 8CER are displayed in Table 7 and Figures 11, S20 – S25.

All compounds **1** – **4** have negative binding energies values as –7.83 kcal/mol (for 4QWO) / –7.51 kcal/mol (for 8CER), –6.41 / –5.53), –8.59 / –6.28 and –6.94 / –7.01 kcal/mol, respectively, and thus a binding affinity to the target protein. The Co^{2+} complex **3** (for 4QWO) and the ligand **1** (for 8CER) have the largest negative binding affinity, so they can be further studied as potential drug molecules to treat the Mpox virus. Reported Mpox drugs such as Tecovirimat and Brincidofovir have binding energies of –9.6 kcal/mol and –9.8 kcal/mol (for 4QWO), respectively[42b], somewhat more negative than those of **1** – **4**.

The most important interactions between **1** – **4** and the studied target proteins are those formed between the amino acid residue ARG A:122 and ASP A:123 of 4QWO with the P═S group and between ARG A:115, VAL A:95 and ASP A:123 with the aromatic rings for compound **1**. In the case of target protein 8CER, interactions between the P═S group of **1** with the amino acid residue PHE B:115, the aromatic rings with GLY B:96, and the N–H unit with ASP B:95 are found.

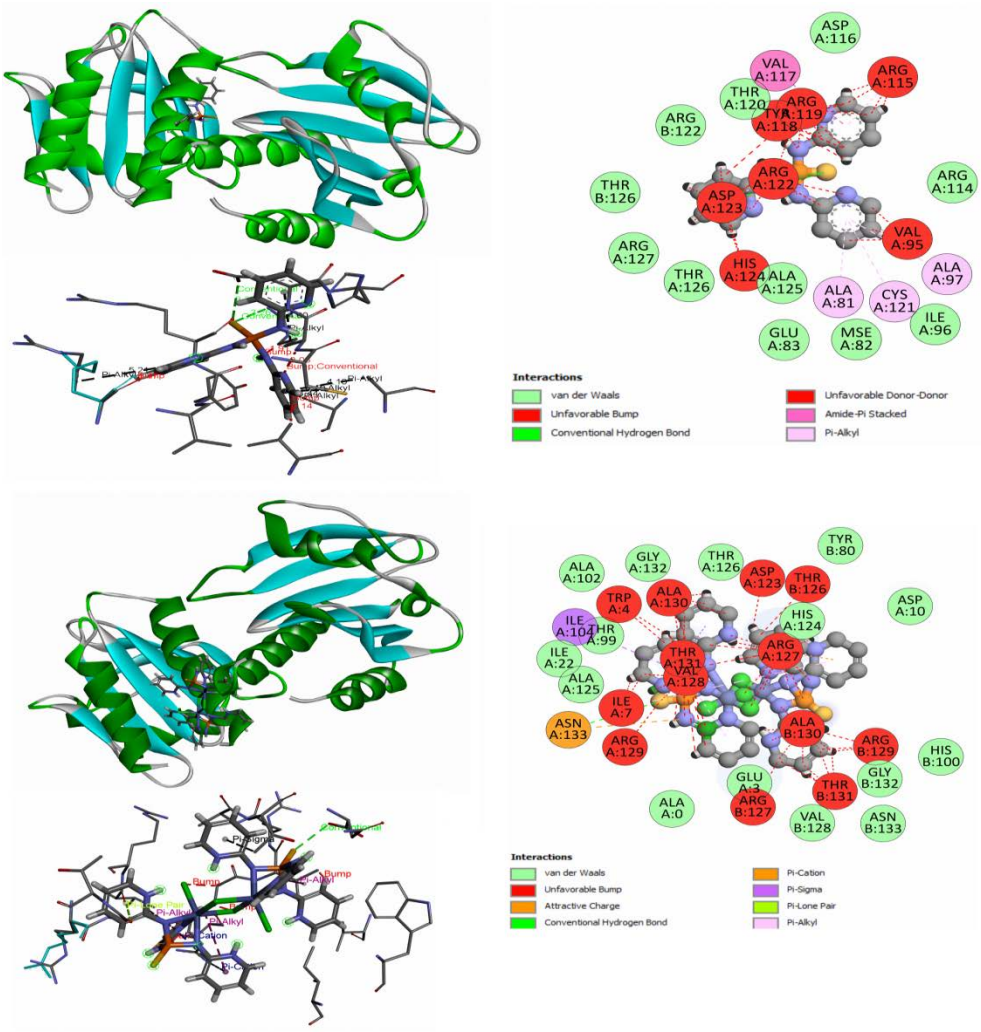

FIGURE 11 Visual description of the 2D and 3D representation maps of the compound **1** (up) and **2** (down) in the best position relative to 4QWO showing the highest negative binding affinity.

TABLE 7 Affinity energies (kcal/mol) and molecular docking interactions between the biological Monkeypox targets (4QWO and 8CER) with the compounds **1** – **4** (ligands).

Receptor	Ligand	Affinity energy	Interaction	Interacted amino acid residue
Monkeypox				
4QWO	**1**	–7.83	van der Waals	ASP A:116, THR A:120, ARG B:122, THR B:126, ARG A:127, ARG A:114, THR A:126, ALA A:125, GLU A:83, MSE A:82, ILE A:96
			Unfavorable bump/donor-donor	ARG A:115, ARG A:119, TYP A:118, ARG A:122, ASP A:123, HIS A:124, VAL A:95
			Amid-π stacked	VAL A:117
			π-Alkyl	ALA A:81, GYS A:121, ALA A:97
	2	–8.59	van der Waals	ALA A:102, GLY A:132, THR A:126, TYR B:80, ASP A:10, THR A:99,ILE A:22, ALA A:125, ALA A:0, GLU A:3, GLY B:132, VAL B:128, ASN B:133, HIS B:100
			Unfavorable bump	TRP A:4, ALA A:130, ASP A:123, THR A:126, THR A:131, VAL A:128, ARG A:127, ILE A:7, ARG A:129
			Attractive charge	ASN A:133
			π-sigma	ILE A:104
	3	–6.50	van der Waals	PRO A:60, GLU A:47, PHE A:66, GLY A:46, LYS A:59,

				ASN A:54, LEU A:58
			Conventional hydrogen bond	LEU A:61
			π-Alkyl	PRO A:50, ILE A:57
	4	–8.89	van der Waals	ASP A:123, THR A:120, GLY B:132, TYR B:80, THR B:126, HIS A:124, GLU B:77, ASN B:78
			Conventional hydrogen bond	HIS B:100, ASN A:14
			Attractive charge	ARG B:129, ASP A:10, ARG A:127
			π-sulfur	PHE A:17
			Alkyl, π-Alkyl	ARG A:119, LYS A:13, ALA B:130
8CER				
	1	–7.51	van der Waals	ALA B:70, ARG B:97, LEU A:154, PHE B:115, SER B:141, GLY B:68, ASP B:138, ARG B:114, ILE B:67, ILE B:94
			Conventional hydrogen bond	ARG A:140
			Attractive charge	ASP B:95
			π-Alkyl	VAL B:116, VAL B:139, ALA A:158
			π-sigma	GLY B:96
	2	–6.28	van der Waals	LYS B:186, THR A:150, GLN A:183, ILE A:185, LEU B:159, LYS A:226, ASP A:182, VAL B:162, PHE B:115, LYS A:186, GLU B:118, ASP B:117
			Conventional hydrogen bond	TRP A:184, SER B:155
			Alkyl	ALA B:158, LEU B:154
	3	–5.53	van der Waals	SER A:141, ASN A:156, SER A:155, TYR B:120, GLN B:127, VAL A:139, VAL B:112, VAL A:116, ASP A:117, GLU A:118
			Conventional hydrogen bond	THR B:113
			π-Alkyl	LEU A:159
			π-cation	ARG B:114, PHE A:115
	4	–7.01	van der Waals	LYS B:186, THR A:150, LYS A:226, GLN A:183, ASP B:117, GLU B:118, VAL B:162, LEU B:159, PHE B:115, ILE A:185
			Conventional hydrogen bond	SER B:155, ASP A:182, TRP A:184
			Alkyl, π-Alkyl	LEU B:154, ALA B:158, LYS A:186

In summary, the following results can be derived from these molecular docking studies.

1. In the case of DNA receptors (1BNA and 4FM9), the Co^{2+} complex **3** and the SPT ligand show a better docking score with binding energies about –8 kcal/mol. The order of the binding energies for the studied compounds is as follows: **3** > **1** > **4** > **2** for 1BNA and **1** > **3** > **4** > **2** for 4FM9.

2. In the case of SARS-CoV-2 receptors, the order of the binding energies is as follows: **1** > **4** > **2** > **3** for 6LU7 with a maximum binding energy about –8 kcal/mol and as **4** > **2** > **1** > **3** for 6M03 with maximum binding energy about –9 kcal/mol. In other words, the Cd^{2+} complex **4** is a better candidate to inhibit coronavirus.

3. In the case of Monkeypox receptors, the order of the binding energies is as follows: **4** > **2** > **1** > **3** for 4QWO with a maximum binding energy about –9 kcal/mol and **1** > **4** > **2** > **3**

for 8CER with a maximum binding energy about –8 kcal/mol. So, the Cd^{2+} complex **4** represents a better inhibitory potential against Mpox virus.

4. Thiophosphory group and pyridine rings are the most important sites of the studied structures that interact with protein pockets by various interactions.

5. The *in silico* docking approach confirms the activity of the compounds **1** – **4** in controlling cancer cells which is in line with *in vitro* results, and the Co^{2+} complex **3** is found as the best option.

6. The order of the best binding energy for the Co^{2+} and Cd^{2+} complexes **2** and **4** is similar and as follows: SARA-CoV-2 > Mpox > DNA, while for ligand **1** and the Co^{2+} complex **3** it is different with DNA > SARA-CoV-2 > Mpox for **1**, Mpox > DNA > SARA-CoV-2 for **3**.

7. The inhibitory activity of the studied compounds against the selected protein viruses (corona and Mpox) is comparable to that of the reported drugs.

8. In general, it is found that the two-nuclear Cd^{2+} complex **4** shows a better potential as anti-viral (corona and Mpox). However, the mono-nuclear Co^{2+} complex **3** has a slightly higher potential for DNA-interaction compared to **4**. It can be expected since Cd^{2+} is among the heavy metals that strongly interfere with proteins which can lead to genotoxicity and oxidative stress[43].

4 CONCLUSION

In the present study, a new thiophosphoramide ligand $P(S)[NH\text{-}^{2}Py]_3$ (**1**) and three novel mono- and bi-nuclear Co^{2+} (**2** and **3**) and Cd^{2+} (**4**) metal complexes derived from it were synthesized and characterized by single-crystal X-ray diffraction. Intermolecular interactions and packing features of the determined structures **1** – **4** were investigated based on the determined structural models and by Hirshfeld surface analysis. The synthesized compounds were *in vitro* studied as anticancer agents against MDA-MB-231 cancer cell lines. The obtained data confirm a suitable inhibitory effect for all compounds, where the Co^{2+} complex **3** with IC50 = 62 ± 1.4 nmolar has the best inhibitory activity against cancer cells. Antioxidant and hemolysis properties of **1** – **4** were also *in vitro* investigated suggesting the use of these compounds as antioxidant and hemolysis inhibitors, especially the Cd^{2+} complex **4**. Furthermore, the studied compounds were used as input models for molecular docking simulations on DNA, SARS-CoV-2 and Monkeypox. The DNA docking simulations on **1** – **4** are in line with the MTT experimental observations, and complex **3** is found as the best

candidate for anti-cancer potential. In the case of antiviral activity, all four compounds can be suggested as potential candidate molecules against SARS-CoV-2 and Mpox, with ligand **1** and Cd^{2+} complex **4** giving the best results.

SUPPLEMENTARY MATERIAL

CCDC numbers 2174158, 2249831, 2261634 and 2261633 for the four reported structures (**1** – **4**) contain the supplementary crystallographic data for this paper. These data can be obtained free of charge from Cambridge Crystallographic Data Centre via www.ccdc.cam.ac.uk/data_request/cif. Supplementary data to this article can be found online at https://….

ACKNOWLEDGEMENTS

Support of this investigation by Semnan University is gratefully acknowledged.

CONFLICT OF INTEREST

Author declare no potential conflict of interest.

DATA AVAILABILITY STATEMENT

Data openly available in a public repository that issues datasets with DOIs.

REFERENCES

[1] aC. Ausín, A. Grajkowski, J. Cieślak, S. L. Beaucage, *Curr. Protoc. in Nucleic Acid Chem.* **2006**, *26*, Chapter 13:Unit 13.16; bK. Uglyanitsa, L. Nefyodov, Y. Doroshenko, J. Nowicky, I. Volchek, W. Brzosko, Y. J. Hodysh, *Drugs Exp. Clin. Res.* **2000**, *26*, 341-356; cE. Procházková, H. Hřebabecký, M. Dejmek, M. Šála, M. Šmídková, E. Tloušťová, E. Zbornikova, L. Eyer, D. Růžek, R. Nencka, *Bioorg. Med. Chem. Lett.* **2020**, *30*, 126897; dD. A. Bakhotmah, *Phosphorus Sulfur Silicon Relat. Elem.* **2020**, *195*, 437-453.

[2] aJ. Y. Shim, Y. A. Kim, Y. T. Lee, B. D. Hammock, H.-S. Lee, *J. Agric. Food Chem.* **2010**, *58*, 5241-5247; bA. Lu, Y. Ma, Z. Wang, Z. Zhou, Q. Wang, *J. Agric. Food Chem.* **2015**, *63*, 9435-9440.

[3] aV. Chandrasekhar, M. D. Pandey, K. Gopal, R. Azhakar, *Dalton Trans.* **2011**, *40*, 7873-7878; bA. Yadav, A. K. Srivastava, A. Balamurugan, R. Boomishankar, *Dalton Trans.* **2014**, *43*, 8166-8169; cA. Ziegler, V. Botha, I. Haiduc, *Inorganica Chim. Acta* **1975**, *15*, 123-128.

[4] aY. Matsumoto, T. Yamamoto, K. Nakano, H. Takatsu, T. Murakami, K. Hongo, R. Maezono, H. Ogino, D. Song, C. M. Brown, *Angew. Chem., Int. Ed.* **2019**, *58*, 756-759; bA. Yadav, A. K. Srivastava, P. Kulkarni, P. Divya, A. Steiner, B. Praveenkumar, R. Boomishankar, *J. Mater. Chem. C* **2017**, *5*, 10624-10629; cY.

Zhao, M. Yu, C. Liu, S. Li, Z. Li, F. Jiang, L. Chen, M. Hong, *J. Mater. Chem. C* **2021**, *9*, 2890-2897.
[5] aP. Carracedo-Reboredo, J. Liñares-Blanco, N. Rodríguez-Fernández, F. Cedrón, F. J. Novoa, A. Carballal, V. Maojo, A. Pazos, C. Fernandez-Lozano, *Comput. Struct. Biotechnol. J.* **2021**, *19*, 4538-4558; bJ. G. Lombardino, J. A. Lowe III, *Nat. Rev. Drug Discov.* **2004**, *3*, 853-862; cH. Zheng, J. Hou, M. D. Zimmerman, A. Wlodawer, W. Minor, *Expert Opin. Drug Deliv.* **2014**, *9*, 125-137; dP. Peluso, B. Chankvetadze, *J. Pharm. Biomed. Anal.* **2024**, *238*, 115836.
[6] aC.-C. Lai, C.-K. Hsu, M.-Y. Yen, P.-I. Lee, W.-C. Ko, P.-R. Hsueh, *J. Microbiol. Immunol. Infect.* **2022**, *55*, 787–794; bM. Lv, X. Luo, J. Estill, Y. Liu, M. Ren, J. Wang, Q. Wang, S. Zhao, X. Wang, S. Yang, *Euro Surveill.* **2020**, *25*, 2000125; cE. J. Sohn, J. C. Rotondo, *Genet. Res.* **2023**, e15.
[7] aK. Spiegel, A. Magistrato, *Org. Biomol. Chem.* **2006**, *4*, 2507-2517; bB. C. Baguley, C. J. Drummond, Y. Y. Chen, G. J. Finlay, *Molecules* **2021**, *26*, 552-560.
[8] Agilent, *CrysAlisPRO Version 1.171.38.43c*, Agilent Technologies, Yarnto Oxfordshire, England, **2011**.
[9] A. van der Lee, *J. Appl. Crystallogr.* **2013**, *46*, 1306-1315.
[10] L. Palatinus, G. Chapuis, *J. Appl. Crystallogr.* **2007**, *40*, 786-790.
[11] P. W. Betteridge, J. R. Carruthers, R. I. Cooper, K. Prout, D. J. Watkin, *J. Appl. Crystallogr.* **2003**, *36*, 1487.
[12] R. I. Cooper, A. L. Thompson, D. J. Watkin, *J. Appl. Crystallogr.* **2010**, *43*, 1100-1107.
[13] A. L. Spek, *Acta Crystallogr. Sect. D* **2009**, *65*, 148-155.
[14] C. F. Macrae, I. J. Bruno, J. A. Chisholm, P. R. Edgington, P. McCabe, E. Pidcock, L. Rodriguez-Monge, R. Taylor, J. Streek, P. A. Wood, *J. Appl. Crystallogr.* **2008**, *41*, 466-470.
[15] P. R. Spackman, M. J. Turner, J. J. McKinnon, S. K. Wolff, D. J. Grimwood, D. Jayatilaka, M. A. Spackman, *J. Appl. Crystallogr.* **2021**, *54*, 1006-1011.
[16] J. J. McKinnon, D. Jayatilaka, M. A. Spackman, *ChemComm* **2007**, 3814-3816.
[17] M. A. Spackman, J. J. McKinnon, *CrystEngComm* **2002**, *4*, 378-392.
[18] M. A. Spackman, J. J. McKinnon, D. Jayatilaka, *CrystEngComm* **2008**, *10*, 377-388.
[19] J. J. McKinnon, M. A. Spackman, A. S. Mitchell, *Acta Crystallogr. Sect. B* **2004**, *60*, 627-668.
[20] C. Jelsch, K. Ejsmont, L. Huder, *IUCrJ* **2014**, *1*, 119-128.
[21] Z. Abbasi, M. Salehi, M. Kubicki, A. Khaleghian, *J. Coord. Chem.* **2017**, *70*, 3132-3146.
[22] L. Ghasemi, M. Behzad, A. Khaleghian, A. Abbasi, A. Abedi, *Appl. Organomet. Chem.* **2022**, *36*, e6639.
[23] aJ. C. Fernandes, P. Eaton, H. Nascimento, M. S. Gião, Ó. S. Ramos, L. Belo, A. Santos-Silva, M. E. Pintado, F. X. Malcata, *Carbohydr. Polym.* **2010**, *79*, 1101-1106; bA. Talebi, M. Salehi, A. Khaleghian, M. Kubicki, *Inorganica Chim. Acta* **2023**, *546*, 121296.
[24] M. Iraji, A. Khaleghian, R. E. Malekshah, M. Abbasi, D. Basir, *J. Drug Deliv. Technol.* **2023**, *85*, 104528.
[25] F. Stanzione, I. Giangreco, J. C. Cole, *Progr. Med. Chem.* **2021**, *60*, 273-343.
[26] G. M. Morris, R. Huey, W. Lindstrom, M. F. Sanner, R. K. Belew, D. S. Goodsell, A. J. Olson, *J Comput. Chem.* **2009**, *30*, 2785-2791.
[27] M. Taherzadeh, M. Pourayoubi, M. Nečas, *Phosphorus Sulfur Silicon Relat. Elem.* **2019**, *194*, 39-46.

[28] aM. Najarianzadeh, A. Tarahhomi, S. Pishgo, A. van Der Lee, *Appl. Organomet. Chem.* **2022**, *36*, e6636; bM. Sebghati, A. Tarahhomi, M. S. Bozorgvar, D. G. Dumitrescu, A. van Der Lee, *RSC Adv.* **2021**, *11*, 8178-8197.
[29] C. R. Groom, I. J. Bruno, M. P. Lightfoot, S. C. Ward, *Acta Crystallogr. Sec. B* **2016**, *72*, 171-179.
[30] V. Chandrasekhar, M. D. Pandey, K. Gopal, R. Azhakar, *Dalton Trans.* **2011**, *40*, 7873-7878.
[31] F. Ebnou, M. M'Haiham, K. Ebeid, C. L. Carpenter-Warren, A. M. Slawin, J. D. Woollins, M. T. B. Dhia, M. A. Sanhoury, *Polyhedron* **2019**, *159*, 206-211.
[32] K. Ebeid, F. Ebnou, M. M'haiham, C. Carpenter-Warren, A. Slawin, J. Woollins, M. Ben Dhia, A. Barry, M. Sanhoury, *J. Coord. Chem.* **2021**, *74*, 2670-2681.
[33] aA. K. Gupta, A. K. Srivastava, I. K. Mahawar, R. Boomishankar, *Cryst. Growth Des.* **2014**, *14*, 1701-1709; bA. K. Gupta, S. S. Nagarkar, R. Boomishankar, *Dalton Trans.* **2013**, *42*, 10964-10970.
[34] aT. Davenport, T. Tilley, *Dalton Trans.* **2015**, *44*, 12244-12255; bS. Alvarez, *Chem. Rev.* **2015**, *115*, 13447-13483; cN. Sinha, S. Kumar, D. Kumar, C. M. Chandra, S. Kumar, S. Sharma, *Asian J. Chem.* **2018**, *30*, 2424-2428.
[35] H. Seker, B. Bertram, A. Bürkle, B. Kaina, J. Pohl, H. Koepsell, M. Wießler, *Br. J. Cancer* **2000**, *82*, 629-634.
[36] L. Ghasemi, M. H. Esfahani, U. Sahebi, A. Divsalar, A. Abbasi, M. Behzad, *J. Mol. Struct.* **2023**, *1294*, 136568.
[37] A. D. Demirag, S. Çelik, S. Akyüz, A. Özel, *Süleyman Demirel Univ. Fen Bilim. Enst. Derg.* **2021**, *25*, 539-547.
[38] D. M. Khaled, M. E. Elshakre, M. A. Noamaan, H. Butt, M. M. Abdel Fattah, D. A. Gaber, *Int. J. Mol. Sci.* **2022**, *23*, 11799.
[39] L. Ghasemi, A. Abedi, A. Abbasi, M. Kucerakova, M. Dusek, M. Behzad, *Inorg. Chem. Commun.* **2024**, *159*, 111795.
[40] R. R. Deshpande, A. P. Tiwari, N. Nyayanit, M. Modak, *Eur. J. Pharmacol.* **2020**, *886*, 173430.
[41] aM. V. Arasu, P. Vijayaragavan, S. Purushothaman, M. Rathi, N. A. Al-Dhabi, V. Gopalakrishnan, K. C. Choi, S. Ilavenil, *J. Infect. Public. Heal.* **2023**, *16*, 784-791; bH. Harapan, Y. Ophinni, D. Megawati, A. Frediansyah, S. S. Mamada, M. Salampe, T. Bin Emran, W. Winardi, R. Fathima, S. Sirinam, *Viruses* **2022**, *14*, 2155.
[42] aY. Ophinni, A. Frediansyah, S. Sirinam, D. Megawati, A. M. Stoian, S. S. Enitan, R. Y. Akele, R. Sah, K. Pongpirul, Z. Abdeen, *Narra J* **2022**, *2*; bM. K. Dassanayake, T.-J. Khoo, C. H. Chong, P. Di Martino, *Int. J. Mol. Sci.* **2022**, *23*, 11131.
[43] C. S. Tzima, C. N. Banti, S. K. Hadjikakou, *J. Biol. Inorg. Chem.* **2022**, *27*, 611-629.